Organisms employ a mode-switching strategy for solving the explore-vs-exploit problem

Debojyoti Biswas[1], Andrew Lamperski[2], Yu Yang[3], Kathleen Hoffman[4], John Guckenheimer[5], Eric S. Fortune[6], and Noah J. Cowan[1,3,*]

[1]Laboratory for Computational Sensing and Robotics, Johns Hopkins University, Baltimore, MD, USA.
[2]Department of Electrical and Computer Engineering, University of Minnesota, Minneapolis, MN, USA.
[3]Department of Mechanical Engineering, Johns Hopkins University, Baltimore, MD, USA.
[4]Department of Mathematics and Statistics, University of Maryland, Baltimore County, Baltimore, MD, USA.
[5]Department of Mathematics, Cornell University, Ithaca, NY, USA.
[6]Federated Department of Biological Sciences, New Jersey Institute of Technology, Newark, NJ, USA.
[*]e-mail: ncowan@jhu.edu

Abstract

Movement and sensing are linked in organisms as their sensors are embedded in their bodies. This inescapable link results in a behavioral conflict between producing costly movements for gathering information ("explore") [1–3] versus using previously acquired information to achieve a goal ("exploit") [4]. Optimally trading-off exploration and exploitation is an intractable problem [5–7], and the strategies that animals utilize to resolve this conflict are poorly understood [8]. Here we show that weakly electric fish (*Eigenmannia virescens*) [2, 3, 9] use a mode-switching strategy that solves the explore–exploit conflict [8] during a refuge tracking task [10–13] and show that this strategy is modulated by sensory salience. Fish produced distinctive non-Gaussian (i.e., non-normal) distributions of movement velocities characterized by sharp peaks for slower, task-oriented "exploit" movements and broad shoulders for faster, "explore" movements. Surprisingly, measures of non-normality increased (rather than decreased) in relation to increased sensory salience. Reanalysis of published data revealed that this distinctive distribution of movement velocities is produced by phylogenetically diverse organisms, from amoeba to humans. Further, other species exhibited the same counter-intuitive modulation of mode-switching in relation to sensory salience. We propose a parsimonious, state-uncertainty based mode-switching heuristic that reproduces the distinctive velocity distribution and explains its relationship to sensory salience. This mode-switching strategy likely manifests in diverse biological mechanisms, from cellular processes for single-cell motility to network-level processes for the control of movement in animals.

Main

Organisms display complex patterns of movement that arise from the interplay between obtaining task-relevant information ("explore") and putting current information to use ("exploit"). Exploratory movements (gaining information) and exploitative movements (achieving the task at hand) serve distinct roles, despite often being mediated via the same motor systems. For example, during refuge tracking, weakly electric fish (*Eigenmannia virescens*) produce both information-seeking exploratory movements [2, 3, 9]

and goal-driven exploitative movements [10, 13] using the same locomotor system [14, 15]. Critically, this behavior illustrates how explore and exploit movements are often in conflict with one another: fish produce back-and-forth exploratory movements [2, 3, 9] to detect and maintain their position within a stationary refuge.

Resolving the conflict between energetically costly explore movements [9] versus goal-directed exploit movements is a computationally intractable optimization problem [5–7]. How do organisms resolve this conflict? A simple but effective solution to this problem would be for an organism to continuously perform small exploratory sensing movements, while superimposing goal-directed, task-oriented movements. Indeed, this heuristic has proven extremely successful for decades as an engineering approach to solve the explore–exploit problem of identifying states and parameters of a dynamical system during task execution [16]. Such a strategy would produce movement statistics that correspond to a single behavioral mode.

In contrast, we discovered that *Eigenmannia virescens* exhibit fast and slow behavioral modes and that mode switching is modulated by sensory salience in a counter-intuitive manner (Fig. 1–2). Based on an extensive reanalysis of data from the literature (Fig. 3), we found that such mode switching—and its counter-intuitive sensory dependence—is found across taxa, behaviors, and sensory modalities. Finally, we propose an engineering heuristic for selecting modes based on state uncertainty (Fig. 4) that captures the key structural features of mode switching found in animals.

Eigenmannia exhibited fast and slow behavioral modes

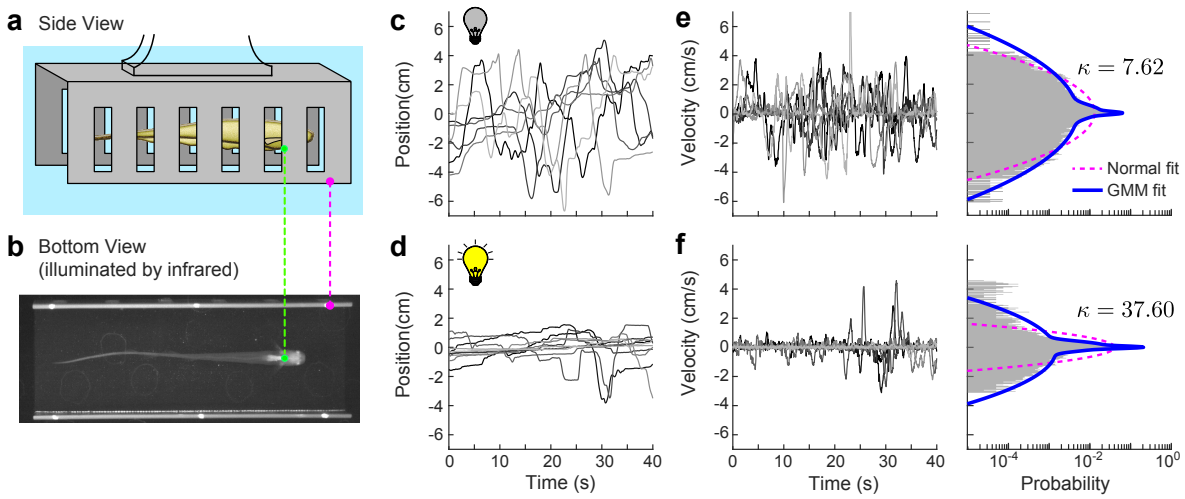

Fig. 1. Velocity distributions are broad-shouldered. (a) Side view (schematic) and (b) bottom view (image) of a fish inside a stationary refuge. The bright ventral patch on the fish (green dot) was tracked as the fish swam inside the refuge (magenta dot). Position traces during (c) lights-off trials ($n = 7$) and (d) lights-on trials ($n = 10$) from a single representative fish. (e) Corresponding velocity traces during lights-off trials (left) and velocity histogram (right) over the same range of velocities, with the kurtosis value κ indicated; note that the time and probability scales of the horizontal axes are shown below panel (f). A three-component Gaussian mixture model (GMM; blue solid curve) fit the data better than the normal fit (magenta dashed curve) as indicated by the lower Kullback-Leibler divergence and Bayesian information criterion values. See Extended Data Table 1 for statistical details. One lights-off trial with large positive velocity is truncated; see Extended Data Fig. 1a,b for full version. (f) Velocity traces of the same fish during lights-on trials (left) and the corresponding histogram (right). Colors and styles of fitting curves are as in panel (e). Again, a GMM was a better fit than a single-component Gaussian.

We examined the behavior of individual *Eigenmannia* as they performed untrained station keeping within a stationary refuge. The task of station keeping requires no movement; hence, significant movements by the fish can largely be attributed to information-seeking, exploratory movements [2, 3, 9]. *Eigenmannia* use both vision and electrosense for station-keeping [12], and varying the lighting provides

an experimental mechanism to examine the effect of visual salience on the selection between explore and exploit movements. We measured the movements of individuals ($N = 5$) in 40 s duration of station-keeping trials in two lighting conditions (between 7 and 10 trials per condition). Lights "on" trials had bright illumination (∼80 lux) and lights "off" trials had low illumination (∼0.3 lux). The order of lights-on and lights-off trials were randomized. Trials in which the fish changed its swimming direction or exited the refuge were discarded. Consistent with prior studies [2, 9], fish moved significantly more in lights-off trials than in lights-on trials (Extended Data Fig. 1).

Fish produced movements with different velocities in a pattern that is consistent with a mode-switching strategy. For each lighting condition, the distribution of velocities (v) featured a sharp peak around $v = 0$ with "broad" shoulders for higher positive and negative velocities (Fig. 1e,f, right). These empirical distributions differed from Gaussian in two ways: the distinct central peak and the broad shoulders corresponding to the faster movements. The central peak (near zero velocity) represents a slow mode of movement, and the broad shoulders represent a faster mode of movement. These modes are associated with exploit and explore respectively, as discussed in greater detail, below.

The two modes were significantly better approximated by three-component Gaussian mixture models (GMMs) than single component models (Fig. 1e,f right). Several measures (Extended Data Table. 1) — Kullback-Leibler (K-L) divergence, Bayesian information criterion (BIC), closeness of quantile-quantile (Q-Q) plots to the reference line (Extended Data Fig. 2) showed that the three-component GMM model was significantly better than a single component model. The trend with Akaike information criterion (AIC) values (not shown) was similar to BIC. Finally, we found that the improvements in the fit of GMMs with more than three components were modest (Extended Data Fig. 1f).

Critically, the fast mode movements increased in frequency in lights-off trials, increasing the weight of the "shoulders". For example, Fig. 1e,f show a representative data from one fish, in which there were 48 fast movements in total with lights off (Fig. 1e left) but only 13 fast movements with lights on (Fig. 1f left). However, the overall higher proportion of fast velocities in lights-off trials leads to what might be a surprising result—higher kurtosis values for lights-on versus lights-off trials (Extended Data Fig. 1e). In other words, the increase in frequency of fast motions in the dark leads to a *decrease* in the (relative) prominence of the central, task-oriented velocity peak at $v = 0$, so that the overall distribution is closer to Gaussian, and the kurtosis trends toward 3.

We found that the trend towards a Gaussian distribution of movement velocities in lights-off trials (reduced sensory salience) to be surprising. Exploratory movements for actively sensing the environment are associated with a nonlinear requirement [17, 18] to make movements that are potentially in conflict with task goals. Therefore, our initial hypothesis was that this nonlinearity would produce *increased* deviation from a Gaussian velocity distribution as sensory salience was reduced. Our initial intuition failed because we did not appreciate that decreases in sensory salience drives the selection of explore behavior, but that behavior itself is approximately Gaussian, and ultimately reduces the relative prominence of the task-oriented central peak.

Interestingly, previous experiments that examined exploratory movements in a similar refuge tracking paradigm in *Eigenmannia* show the same relation between sensory salience and changes in velocity traces but for modulations of a different sensory modality [3]. In these previous experiments, artificially generated electrical signals were used to diminish the salience of electrosensory information as electric fish performed refuge tracking. Our reanalysis of these published data (see Supplementary Methods for details) showed that fish exhibited the distinctive non-Gaussian distribution of velocities. Moreover, the velocity distributions were modulated in relation to electrosensory salience: lower kurtosis values (corresponding to more normal distributions) occurred in experimental trials with added artificial electrosensory "jamming" signals (Extended Data Fig. 3).

Sensory salience drives explore–exploit mode switching

How do changes in sensory salience drive changes in mode switching? We segregated the velocity trajectories into two modes: a slow velocity mode and a fast velocity mode comprising both positive and negative movement velocities (Fig. 2a,b, Figure 2—figure supplement 1): slow (orange), fast positive (green), and fast negative (blue) (see Methods for segregation clustering algorithm). In the slow mode, fish were almost stationary, whereas in the fast modes, fish swam in rapid bouts of forward and backward

movement (Fig. 2a,b).

Fish produced slow and fast velocity modes of movements in both lights-on and lights-off trials. Critically, fish switched between slow and fast modes more frequently in lights-off trials than in lights-on trials (Fig. 2c). We computed the residence time in each behavioral mode as a proportion of the total time spent in that mode to the trial duration (40 s) (note that the residence time in slow and fast modes adds up to unity). In lights-on trials, the residence time τ_s in the slow exploit mode was higher (> 1.7 times) than the lights-off trials. In contrast, the residence time in the fast explore modes $(1 - \tau_s)$ was higher in light-off than in lights-on trials.

Additionally, we computed the transition rates between slow (S) and fast (F) modes as a two-state Markov process. We found that the transition rate S $\rightarrow$ F was significantly lower in lights-on versus lights-off trials, i.e. the slow (exploit) state was visited more frequently in the lights-on trials compared to lights-off trials (Figure 2—figure supplement 2).

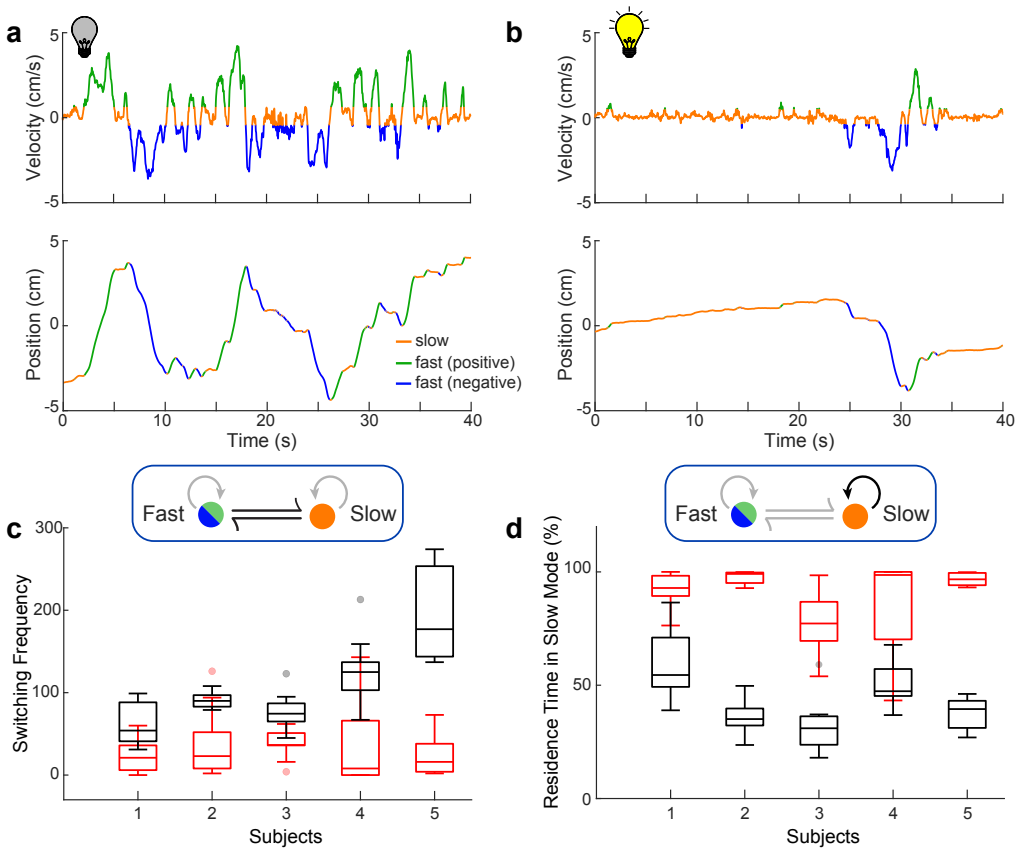

Fig. 2. Bursts of faster movements are more common in lights-off trials. (a,b) Fish exhibited two distinct behavioral modes, slow movement and fast movement, as seen in the velocity (top) and position (bottom) of representative trials from the same fish under lights-off (a) and lights-on (b) conditions. The colors denote different modes: slow (orange), fast positive (green), and fast negative (blue). (c) The switching between the fast (both positive and negative combined) and slow mode was more frequent in lights-off trials (black) as compared to lights-on trials (red). The mean switching frequencies in lights-off trials were significantly higher than the lights-on trials (one-tailed p-value < 0.002). (d) The residence time in the slow mode, computed as the percent of the trial duration (40 s), was higher during lights-on trials (one sided p-value < 0.002 for all subjects). For both (c,d), the p-values were calculated using the Mann-Whitney-Wilcoxon test.

Mode-switching is found across taxa, behaviors, and sensory modalities

Is this mode-switching strategy for solving the explore versus exploit problem found in other species, in other categories of behavioral tasks, and in control systems that rely on other sensing modalities? To answer this question we analyzed published data from a wide phylogenetic range of taxa, from single-celled organisms to humans, involving categorically different tasks and sensorimotor regimes [3, 19–26]. For every example we examined, we found the same distinctive non-normal distribution of velocities with a peak at low velocity movements and broad shoulders for higher velocity movements.

For example, postural sway movements in humans are thought to prevent the fading of postural state information during balance [27]. Our reanalysis of quiescent stance data [25] revealed evidence of mode switching (Fig. 3a) that is remarkably similar to our findings in electric fish. In this task, human subjects used visual and tactile feedback to maintain an upright posture. The distribution of sway velocities revealed the distinct peak at low velocities corresponding to the task goal, and broad shoulders for higher velocities corresponding to exploratory movements; the velocity statistics were better captured by a GMM than a normal distribution. Further, the velocity distribution showed the same surprising relation to changes in salience, becoming more Gaussian when sensory salience was decreased (Extended Data Fig. 6), as seen in *Eigenmannia*.

Mode switching was also observed in invertebrate species. For example, crepuscular hawkmoths (*Manduca sexta*) use somatosensory feedback from their proboscis to detect the curvature of flowers when searching for nectaries [21]. In this search behavior, which has dynamics that are qualitatively similar to vibrissal sensing in rats [28], the moth sweeps its proboscis across the surface of the flower using a combination of slow- and high-velocity movements. As above, our analysis of the distribution of the rate of change of radial orientation angle (angle between the proboscis tip trajectory and radial axis of the flower) before the insertion of the proboscis tip to the nectary shows the characteristic sharp peak with broad-shoulders (Fig. 3g) that is captured by a GMM. Experimental changes in the shape of artificial flowers that degrade the salience of the curvature of the flower surface [21] resulted in a decrease of the kurtosis value of the proboscis angular velocity distribution (Figure 3—figure supplement 7), similar to how both *Eigenmannia* and humans responded to changes in sensory salience.

The fact that this salience-based, mode switching strategy was found in two distantly related taxa performing wildly different behaviors using different sensorimotor systems suggests that the strategy emerged as a convergent solution to the explore versus exploit problem. We found additional evidence of convergence of this solution for the explore versus exploit problem in reanalysis of data from visual saccades in humans (Fig. 3b, Extended Data Fig. 7) [29] and in house mice *Mus musculus* (Fig. 3c, Extended Data Fig. 8), movements of the pinnae of echolocating big brown bats *Eptesicus fuscus* (Fig. 3d, Extended Data Fig. 9) [24], olfaction in Eastern moles *Scalopus aquaticus* (Fig. 3e, Extended Data Fig. 10) [22] and American cockroaches *Periplaneta americana* (Fig. 3f, Extended Data Fig. 11) [19], and visual tracking of a swaying flower in three species of hawkmoths (*Manduca sexta, Deilephila elpenor, Macroglossum stellatarum*) (Fig. 3h, Extended Data Fig. 13) [20].

Intriguingly, our analysis of the dynamics of transverse exploration of pseudopods in amoebae (*Amoeba proteus* and *Metamoeba leningradensis*) reveals similar GMM velocity distributions in response to an electric field (Extended Data Fig. 14) [26]. Although our modeling approach (see next section) includes inertial dynamics that cannot be directly applied to movement of organisms in the low Reynolds number regimes occupied by single-celled and other microscopic organisms, these observations are consistent with a mode-switching strategy for the control of movement.

The examples described above include a broad phylogenetic array of organisms that perform a variety of behavioral tasks using different control and morphophysiological systems. Just as these behavioral systems evolved within each of the lineages represented in our reanalyses, we suggest that mode switching likely evolved independently in each system as well. In other words, the similarities we found across taxa are the result of convergent evolution towards a common solution—mode switching—for the explore versus exploit problem.

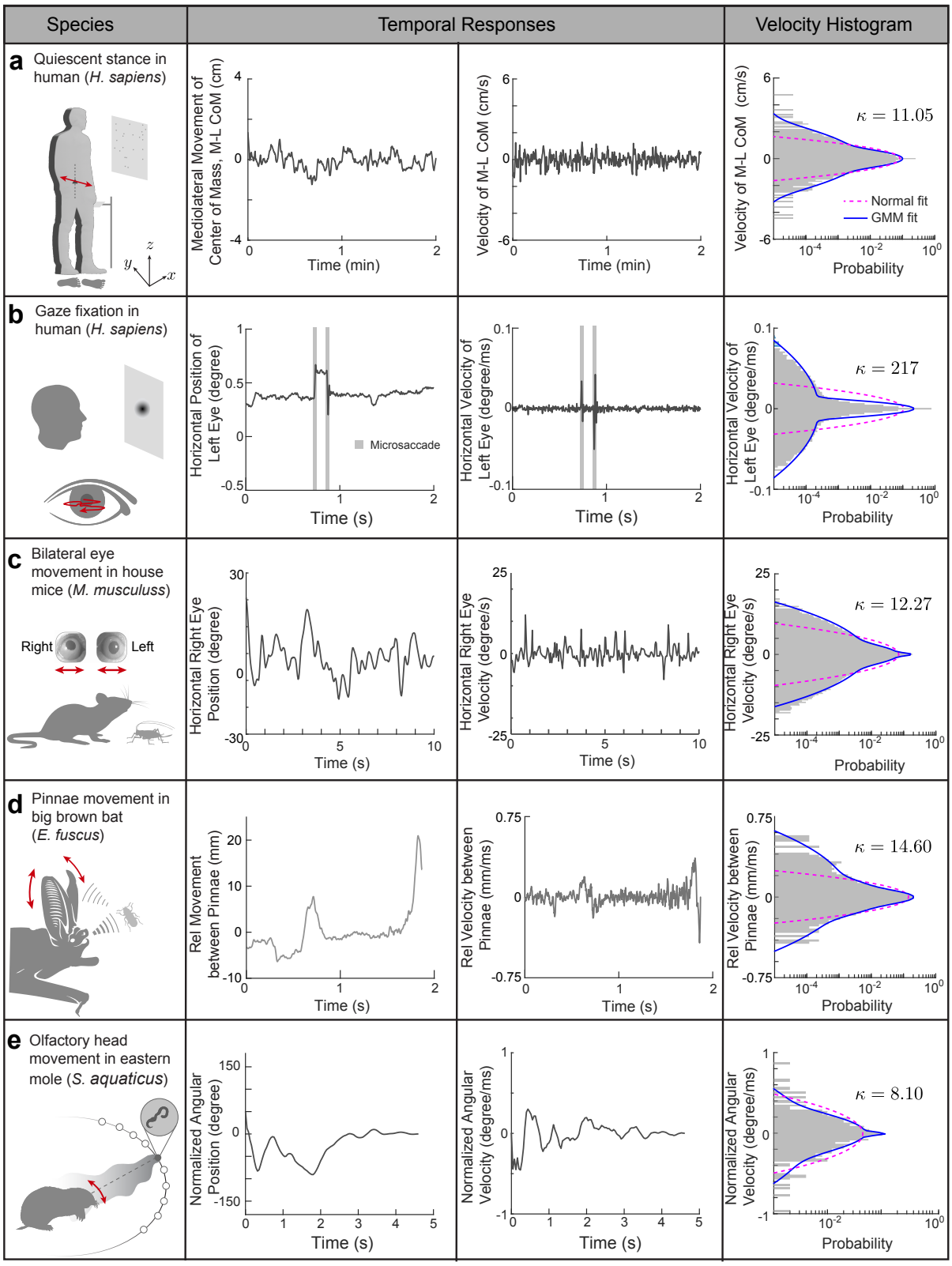
Species
Temporal Responses
Velocity Histogram
a
Quiescent stance in human (H. sapiens)
Mediolateral Movement of Center of Mass, M-L CoM (cm)
Time (min)
Velocity of M-L CoM (cm/s)
Time (min)
Velocity of M-L CoM (cm/s)
κ = 11.05
Normal fit
GMM fit
Probability
b
Gaze fixation in human (H. sapiens)
Horizontal Position of Left Eye (degree)
Microsaccade
Time (s)
Horizontal Velocity of Left Eye (degree/ms)
Time (s)
Horizontal Velocity of Left Eye (degree/ms)
κ = 217
Probability
c
Bilateral eye movement in house mice (M. musculuss)
Right
Left
Horizontal Right Eye Position (degree)
Time (s)
Horizontal Right Eye Velocity (degree/s)
Time (s)
Horizontal Right Eye Velocity (degree/s)
κ = 12.27
Probability
d
Pinnae movement in big brown bat (E. fuscus)
Rel Movement between Pinnae (mm)
Time (s)
Rel Velocity between Pinnae (mm/ms)
Time (s)
Rel Velocity between Pinnae (mm/ms)
κ = 14.60
Probability
e
Olfactory head movement in eastern mole (S. aquaticus)
Normalized Angular Position (degree)
Time (s)
Normalized Angular Velocity (degree/ms)
Time (s)
Normalized Angular Velocity (degree/ms)
κ = 8.10
Probability

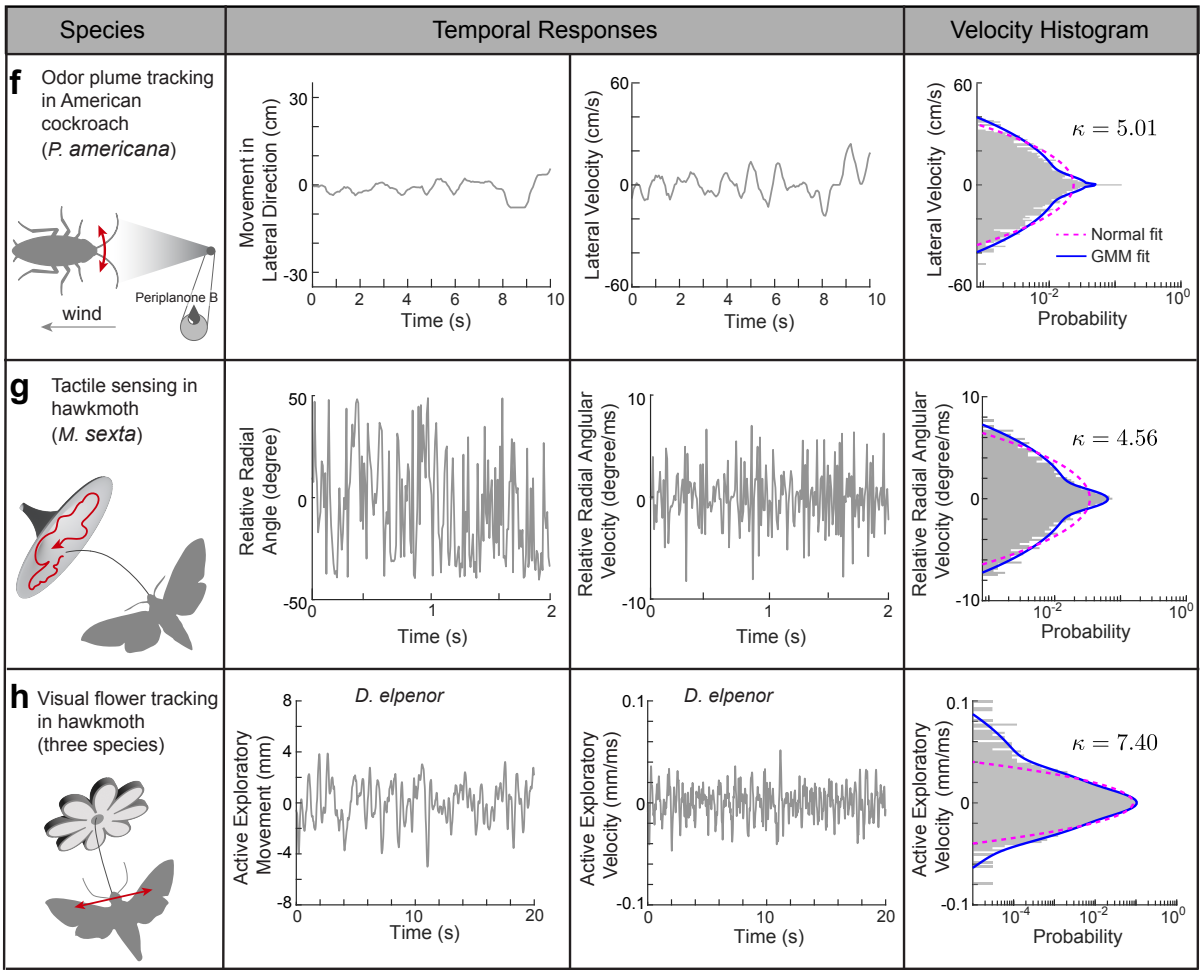

Fig. 3. Mode switching is a robust feature across taxa, behaviors, and sensing modalities. Reanalysis of data from prior studies reveals a conserved statistical structure of movements across a range of behaviors and organisms: (a) postural sway in humans (*Homo sapiens*) during maintenance of quiet upright stance [25], (b) microsaccades in humans (*Homo sapiens*) during fixated gaze [29], (c) bilateral eye movements in mice (*Mus musculus*) during prey (cricket) capture [23], (d) pinnae movements in big brown bats (*Eptesicus fuscus*) while echolocating prey (mealworm) [24], (e) olfactory driven head movements in eastern moles (*Scalopus aquaticus*) in response to food (earthworms) [22], (f) odor plume tracking in American cockroaches (*Periplaneta americana*) in response to sex pheromone (Periplanone B) [19], (g) tactile sensing by hawkmoths (*Manduca sexta*) while searching for a flower nectary [21], and (h) visual tracking of swaying flower by hawkmoths (three species; only data from *Deilephila elpenor* is shown, for the rest see Extended Data Fig. 13) [20]. The second column shows representative temporal traces of the active exploratory movements whereas the third column shows the respective velocity traces. The velocity histograms in the fourth column indicate that, unlike the normal distribution (magenta dashed curve), the three-component Gaussian mixture model (GMM; blue solid curve) captures the broad-shouldered nature of the velocity data across species, behaviors, and sensing modalities. See Extended Data Table 2, Extended Data Table 3 for statistical details. Photo credit: Mice eye image courtesy of authors in [23], published under the terms of the Creative Commons Attribution License.

Explore–Exploit Mode-Switching Strategy

Why might animals use mode switching, rather than the simpler heuristic used by adaptive control engineers [16] of applying continual, low-amplitude exploratory inputs? To address this question, we propose a parsimonious heuristic model that comprises a nonlinear motion-dependent sensor, a linear musculoskeletal plant, a state estimator, and a mode-switching controller (Fig. 4a). The key feature of the model is that the nonlinear sensory system embodies high-pass filtering (i.e., fading or adapting) characteristics found across biological sensory systems [30, 31]. This sensory system model ("motion dependent sensor" in Fig. 4a) assumes nonlinear measurements that decay to zero over time in the face of constant stimuli. Previous theoretical work has demonstrated that exploratory movements are required for state estimation in control systems that rely on such high pass (i.e., fading) sensors [17, 18]. All details of the modeling can be found in the Methods.

The controller includes a state-feedback-based task level component, $-f(\hat{x}, \hat{v})$, that exploits previously collected sensory information; that information is parsimoniously encoded in estimates of the position and velocity $(\hat{x}, \hat{v})$, as well as an ongoing estimate of the covariance of these estimates. It also includes an active control component, $u_a(t)$, that seeks to gain new information through exploratory movements. We tested three exploratory movement heuristics for the controller:

1. **Zero Excitation:** This is a passive strategy (i.e. no exploration) in which the system provides no input excitation for the actuation forces ($u_a(t) = 0$ for all t). This is a conventional state-feedback controller.
2. **Gaussian Excitation:** This scheme tests a common continuous exploration strategy used in the field of adaptive control [16]. The controller continually injects a Gaussian input $u_a(t)$.
3. **Triggered Excitation:** This mode-switching strategy depends on lower and upper thresholds, $T_{\min}$ and $T_{\max}$; the controller only injects Gaussian input when the uncertainty in the state estimator exceeds $T_{\max}$, and then continues to inject input until this uncertainty drops below a lower threshold, $T_{\min}$.

As prior theoretical work shows [18], the Zero Excitation strategy (i.e., traditional state-estimate feedback) is incapable of minimizing the state estimation error (e_{RMS}, Fig. 4b, left), illustrating the need for an additional active sensing component in the face of adaptive sensing and perceptual fading.

The Gaussian Excitation and Triggered Excitation schemes both facilitate substantially better position control (Fig. 4b, middle and right). Though these schemes resulted in comparable state-estimation errors (e_{RMS}, Fig. 4b, middle and right), the triggered excitation proved to be more efficient, requiring substantially lower control effort (u_{RMS} (Fig. 4c, middle and right). Moreover, unlike the Gaussian Excitation scheme, Triggered Excitation generated a distinctive broad-shouldered velocity distribution that featured a sharp peak near zero with broad shoulders corresponding to bursts of fast movement (Fig. 4d, middle and right). This distribution was strikingly similar to experimental observations.

The choice of thresholds in the Triggered Excitation scheme plays an important role; with relatively low thresholds, we can recover statistics that approach that of the Gaussian excitation, whereas appropriately high thresholds lead to velocity distributions with higher kurtosis (departing from normality), while requiring less control effort (Extended Data Fig. 15b–d).

How does sensory salience affect the performance of the Triggered Excitation (mode-switching) heuristic? To simulate the effects of changes in sensory salience, we parametrically varied the amplitude of sensory noise while keeping the switching thresholds $T_{\min}$ and $T_{\max}$ constant. As noise variance was increased, the kurtosis value of the velocity distribution decreased, numerically approaching normality in the limit of high sensory noise (Extended Data Fig. 16).

This trend of decreased kurtosis in the face of increased noise variance captures the widespread observation in animals that velocity statistics tend toward a Gaussian distribution as sensory salience is decreased. Moreover, the detailed mechanism for this, namely that the bursts of exploratory movements became more frequent, matches our experimental observations in *Eigenmannia*, which performed more frequent transitions to fast movements in the lights-off trials, spending less time in the slow mode (Fig. 2c,d). These analyses clarify that this trend toward Gaussian with decreased salience is an epiphenomenon of mode-switching: as the frequency of fast movement bursts increases, it overwhelms the task-oriented movements, diminishing the prominence of the central peak.

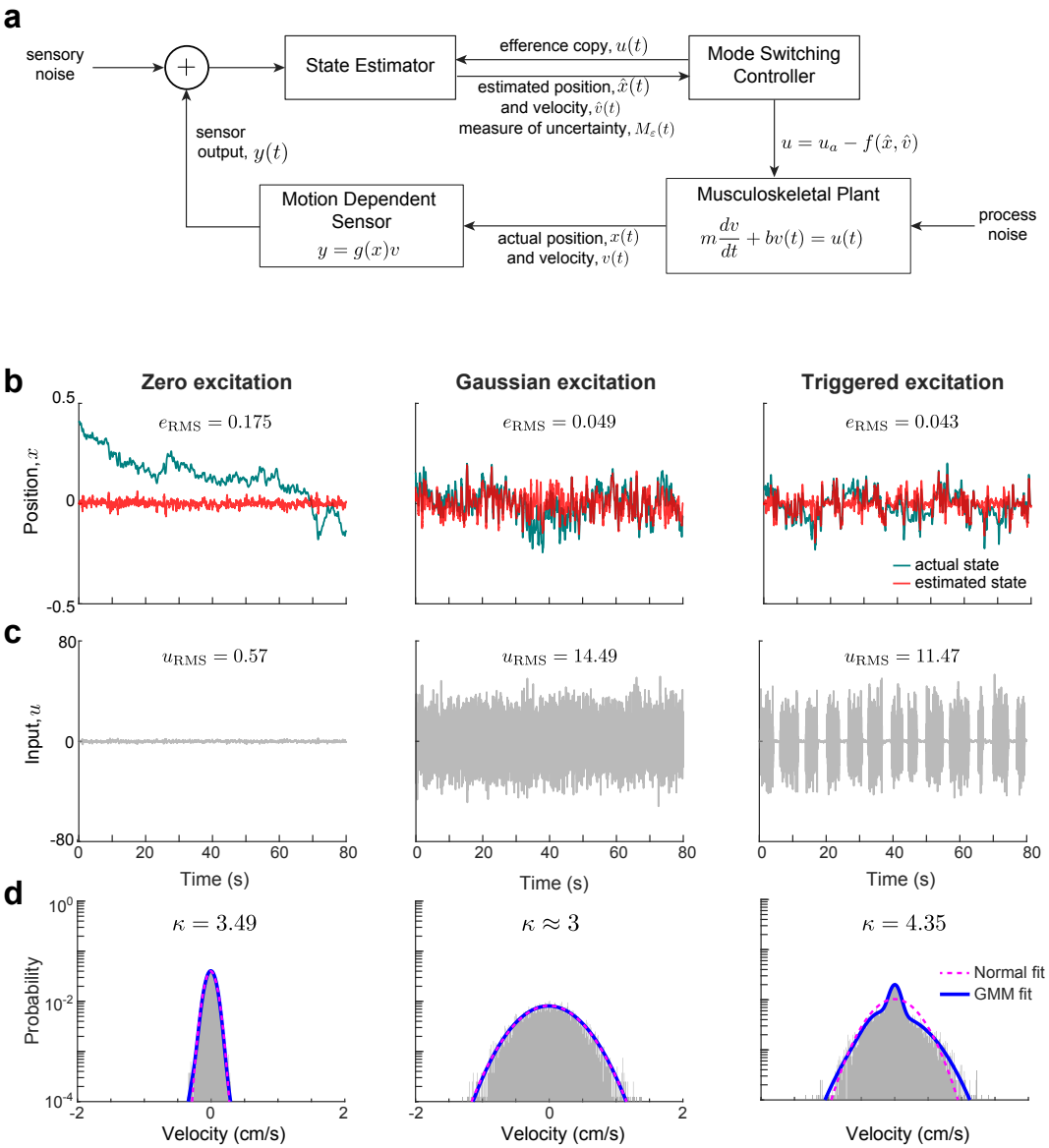

Fig. 4. Template model illustrating different exploration strategies. (a) Schematic of a mode-switching strategy. The musculoskeletal plant for animal locomotion includes two states—position (x) and velocity (v). The state estimator has access to noisy measurements from a nonlinear adaptive sensor ($g(x)v$). The state estimator (extended Kalman filter) is designed to work in tandem with the mode switching controller. The controller output, u comprises both state-feedback ($-f(\hat{x}, \hat{v})$) and an active control component ($u_a(t)$). See Methods for details. (b) Simulated position traces (actual states: teal, estimated states: red) using different exploratory movement strategies for $u_a(t)$: zero excitation (left), continuous Gaussian excitation (middle), and triggered excitation (right) along with the state-feedback. Both continuous Gaussian and triggered excitation inject Gaussian input, except that the triggered strategy only injects the Gaussian signal when the measure of uncertainty (M_ε) reaches a threshold (see Methods). Respective RMS values of the state estimation error (e_{RMS}) are shown in the panels. (c,d) Controller input traces (c) and the velocity histograms for various schemes as in (b). Respective RMS values of the inputs (u_{RMS}) are shown on the panels of (c). Note that the triggered excitation scheme achieves comparable positional estimation error despite substantially lower input energy. In (d) the fits with a normal distribution (magenta dashed) and three-component Gaussian mixture model (blue solid) are shown along with the respective kurtosis (κ) values.

Discussion

We showed that the velocity distributions of exploratory movements are broad-shouldered across taxa and that this distinctive distribution of movements is robustly modulated by the sensory salience. The bouts of ancillary movements that comprise the broad shoulders of these velocity distributions are commonly described as "active sensing", i.e., the expenditure of energy by organisms for the purpose of sensing [32][1]. J.J. Gibson popularized active sensing research over 50 years ago in humans in relation to touch [1], but the original ideas date back at least to the 18th century (for a historical account, see [32]).

Surprisingly, active sensing is largely avoided in engineering design despite being ubiquitous in animals. The performance of engineered systems may benefit from the generation of movement for improved sensing. An algorithm known as Ergodic Information Harvesting (EIH) [3] could be used to control movements for sensing in artificial systems. This algorithm balances the energetic costs of generating movements against the expected reduction in sensory entropy. EIH was tested in relation to several animal model systems, and produces plausible animal trajectories [3].

Interestingly, the EIH algorithm produces the opposite trend in kurtosis of velocity distributions in relation to sensory salience that we observed here (Extended Data Table. 4): as sensory salience decreases, there is an increase in active sensing movements but a decrease in kurtosis. That EIH leads to decrease in kurtosis occurs in part because EIH generates continuous sensing movements and does not incorporate mode switching. A refined EIH model that generates the temporally distinct epochs of sensing movements that characterize mode switching will better reflect our findings in animals, and is a promising strategy for improving the performance of robotic control systems.

How mode switching is manifest across the diverse biological systems we examined is a compelling open question. It is compelling because many of these control systems have evolved via convergent evolution in which adaptive strategies emerge independently across lineages. A result of convergent adaptation is that species often rely on idiosyncratic features, e.g., feathers or skin flaps, to achieve the same adaptive strategy, e.g. flapping flight. The findings presented here demonstrate that mechanisms for mode switching must be present in control systems that range from sub-cellular systems [38] to neural systems in vertebrates and other animals.

The mechanisms for mode switching in vertebrate nervous systems may emerge at different levels within sensorimotor control pathways. For example, neurophysiological recordings show that sensory salience can be encoded in brain circuits via synchronization and desynchronization of spiking activity [39]. Such population coding of salience [40–42], when coupled with a threshold, could trigger discrete bursts of motor activity for sensing [14]. Motor circuits for the production of discrete bursts of movement occur in spinal circuits [43].

These discrete bursts of movements could arise from reflex-like, threshold-based activity in animals, much like how Mauthner cells trigger a cascade of motor activity when sensory inputs exceed a threshold [44]. A key difference would be that the signal in question would arise from an internal representation of sensory uncertainty, rather than overall level of sensory excitation. Such a reflex-like action could produce stereotyped forms of interactions with the external environment in relation to sensing [14].

Environmental noise makes it difficult for organisms to gather sufficient sensory information without making large exploratory movements. But increased exploration would lead to increased energy expenditure, time to task completion and even predation risk. We contend that, rather than continuous exploration, occasional exploratory movements stimulated by internal representations of uncertainty could enable organisms to safely meet sensory demands on a limited energy budget. Our simplified heuristic model provides only a first step at rationalizing this hypothesis. Notwithstanding the limitations of this simplified theory, the ubiquity of mode switching itself, and its specific and strong dependence on sensory salience, is clear. Gaining certainty on what role mode switching behaviors serve—and how they are implemented in diverse biological mechanisms—will require interleaving new experiments aimed at explaining underlying mechanisms with new modeling to understand their purpose.

[1] Active sensing includes not only the sorts of ancillary movements described here, but also the emission of energetically costly signals including electric fields by weakly electric fishes [33] and echolocation calls in dolphins, birds, and bats [34–37]. The emission and reception of these electrical and acoustic signals are also affected by movements of the individual, which has been a focus of our work in electric fishes [2, 9, 14].

Methods

Tracking of weakly electric fish

Subjects

Adult weakly electric glass knifefish *Eigenmannia virescens* (about 10 – 15 cm in length) were obtained from commercial vendors and housed according to the published guidelines [45]. Water temperature of the experimental tank was kept between 24 – 27 °C and the conductivity of water was in the range of between 10 – 150 µS/cm. The fishes were transferred to the experimental tank at 12 – 24 hours before the experiments started so that they could get acclimated to the environment. The experiments were conducted in two illuminance levels—around 0.3 lux (lights off) and 80 lux (lights on). All the experimental procedures were approved by the Johns Hopkins Animal Care and Use Committee and followed guidelines established by the National Research Council and the Society for Neuroscience.

Experimental apparatus and procedure

The experimental apparatus was similar to that used in previous studies [2, 10–12, 14]. See [2] for more detailed description of the apparatus. The refuge was machined from a 152 mm (152.49 ± 0.28) segment of 46.64 × 50.65 (46.64 ± 0.33 × 50.65 ± 0.10) mm gray rectangular PVC tubing and the bottom surface was removed for the camera to record the ventral view of the fish. On both sides of the refuge, a series of six rectangular windows (6 mm in width and spaced 19 mm apart) were machined to provide visual and electrosensory cues. A PC sent designed digitized input stimuli (25 Hz) from LabView (National Instruments, Austin, TX, USA) to a FPGA based controller for a stepper motor (STS-0620-R, HW W Technologies, Inc., Valencia, CA, USA). The stepper motor drove a linear actuator, leading to the one degree of freedom refuge movement in real time. A video camera (pco.1200, PCO AG, Kelheim, Germany) captured fish movements through mirror reflection at 100 Hz. The captured frames (width × height: 1280 pixels × 276 pixels) were saved as 16 bits .tif files via camera application software (pco.camware, PCO AG, Kelheim, Germany).

Each trial lasted for 60 s. During the initial and final 10 s of each trial, the refuge was actuated to follow a 0.45 Hz sinusoidal trajectory, the amplitude of which was gradually increased to 3 cm, and then decreased to 0 at the end of the 10 s interval in a similar fashion as described in Biswas *et al.* [2].

Tracking Algorithms

Capturing animal locomotion at high frame rate enabled us to observe fine details. But with high frame rate, high tracking accuracy becomes an essential requirement as the position and velocity data are likely to be contaminated by measurement noise. To ensure high tracking accuracy, the refuge and fish position were analyzed by custom video tracking software [46] developed by Balázs P. Vágvölgyi from the Laboratory for Computational Sensing and Robotics (LCSR), Johns Hopkins University. This tracking algorithm worked in two phases. The first phase was template matching, which roughly located the targets (fish or refuge). At the first frame of a given video, a rectangular region was manually selected around the target to create a template. On subsequent frames, a neighborhood region around the template (± 20 pixels) from the previous frame was selected for the computation of a normalized 2-D cross-correlation matrix. If the target was found to change its orientation at new frames, before computing the normalized 2-D cross-correlation, the new image frame was first rotated to match the orientation of the template from previous frame. If needed, the areas of the image were sampled (then scaled and interpolated if necessary) with subpixel accuracy. After creating the template, the second phase applied the Levenberg-Marquardt algorithm to find the global maximum of the normalized cross-correlation function. This step produced a match between the template and target at each frame with subpixel accuracy. Extensive preliminary testing and analysis (not included) were performed to confirm that the remaining measurement errors had smaller variance than the stochastic movements of the fish.

Data Processing

The tracking algorithm stored the fish position in both horizontal and vertical directions (originally in pixels along with the respective pixel to meter conversion factor) as well as the angle of orientation (in degree) in .csv files. We used only the data while the refuge was stationary (40 s, 4000 data points in total) for each trial. To further reduce the measurement noise, the position data was filtered through a Butterworth zero-phase distortion filter (`filtfilt` command in MATLAB) with a 15 Hz cutoff frequency. Fish velocity in the horizontal direction was computed as forward differences of the horizontal position time series.

Identification of Behavioral Modes

For the identification of the three behavioral modes—slow, fast positive and fast negative—the velocity data from each individual from lights-on and lights-off trials were clustered separately into three classes using two velocity thresholds, v_L and v_H ($v_L < v_H$). These threshold values were computed by finding the inflection points of the fitted Gaussian mixture model (GMM), f_{GMM}, to the respective velocity data specific to a lighting condition. To numerically identify the inflection points of f_{GMM}, we located the first and the last indices of the array $\frac{f''_{\mathrm{GMM}}}{f_{\mathrm{GMM}}}$ such that the condition $\frac{f''_{\mathrm{GMM}}}{f_{\mathrm{GMM}}} < x$ was satisfied for a given x. This method separated the central peak of the velocity distribution around zero velocity, from the broad shoulders. We chose $x = 0.005$ for all the individuals irrespective of the lighting conditions, except for subject 1 lights-off trials ($x = 0.02$). The different x-value for subject 1 lights-off trials was chosen so that the relative area under the central peak of the distribution was less than 0.6 (similar to other subjects during lights-off trials).

Simulation

For the musculoskeletal plant, we assumed a simplified second-order Newtonian model [17]:

$$\begin{aligned} \frac{dx(t)}{dt} &= v(t), \\ \frac{dv(t)}{dt} &= -\frac{b}{m}v(t) + \frac{1}{m}u(t) + w_1(t). \end{aligned} \tag{1}$$

Here $x(t)$ is dimensionless position, $v(t)$ is dimensionless velocity, $u(t)$ is the controller input, and $w_1(t)$ is process noise. The process noise includes noise due to physical disturbances [47, 48] as well as motor noise [49]. The system parameters m and b represent unitless mass and viscous damping, respectively.

For the "motion dependent sensor", we assumed a nonlinear measurement model [17,18] with sensory noise $w_2(t)$:

$$y(t) = \frac{d}{dt}s(x(t)) + w_2(t) = g(x)v(t) + w_2(t). \tag{2}$$

Here, $s(x)$ is the position dependent sensory scene experienced by the organism. For the present study, we assumed a quadratic sensory scene $s(x) = \frac{1}{2}\alpha x^2 + \beta x$ with nonzero constant sensory scene parameters α and β. This assumption on sensory scene yields $g(x) = \alpha x + \beta$, a linear function of position, x. Due to the presence of the nonlinearity in the measurement, we assumed an extended Kalman filter (EKF) as the state estimator. The mode-switching controller includes a traditional state-estimate-feedback component, $-f(\hat{x}, \hat{v})$, with estimated position and velocity, $(\hat{x}, \hat{v})$, as well as an active control component, $u_a(t)$. For the state-feedback component we assumed $f(\hat{x}, \hat{v}) = k_1\hat{x} + k_2\hat{v}$. In the Triggered Excitation scheme, for the uncertainty measure (M_ε) we used the trace of the state estimation error covariance matrix, $\mathrm{Tr}(P(t))$. When the uncertainty measure $M_\varepsilon(t)$ rose above a maximum threshold, $T_{\max}$, the controller generated $u_a(t)$ as a Gaussian input with fixed power spectral density and it continued to inject the input until $M_\varepsilon(t)$ dropped below a lower threshold, $T_{\min}$. At this point the controller switched back to traditional state-feedback form. For the Gaussian Excitation scheme, the controller continued to inject a Gaussian input $u_a(t)$ for all time. The systems parameters were chosen from [10,17]: $b = 1.7$,

$m = 1$, $\alpha = 3$, $\beta = 5$, $k_1 = m\omega_n^2$, $k_2 = (2m\zeta\omega_n + b)$, $\zeta = 0.56$, $\omega_n = 1.05 \times 2\pi$, $T_{\max} = 0.006$, $T_{\min} = 0.005$. The process noise, $w_1(t)$ and sensor noise, $w_2(t)$ were assumed to be Gaussian noise inputs with variance 0.03 and 10, respectively. Both continuous Gaussian and triggered excitation injected Gaussian white noise of variance 20.

Statistics

All the statistical analysis was performed with Mann-Whitney-Wilcoxon (MWW) test using custom codes written in MATLAB (Mathworks, Natick, MA, USA). For all tests, the significance level was set to 0.05. The experimental and simulation data are provided as either mean plus or minus the standard deviation ($\mu \pm$SD) or mean plus or minus the standard error of the mean ($\mu \pm$SEM).

Data and software availability

Before final submission, an archived version of the datasets and the analysis code supporting this article will be made available through the Johns Hopkins University Data Archive.

Acknowledgement

We thank Tim Kiemel for providing human balance data and Balázs P. Vágvölgyi for the tracking software used in this work. We thank Cynthia F. Moss, Varun Sharma, and Simon Sponberg for suggesting relevant articles for the reanalysis of the locomotion data from different species. This work was supported by Office of Naval Research under grant no. N00014-21-1-2431 (N.J.C).

Author contribution

Conceptualization, all authors; Methodology, all authors; Software, D.B., A.L., K.H., Y.Y. and J.G.; Formal Analysis, D.B., A.L., K.H., Y.Y. and J.G.; Investigation, Y.Y.; Data Curation, D.B. and Y.Y.; Writing – Original Draft, all authors; Writing – Review & Editing, all authors; Visualization, D.B. with other authors; Supervision, N.J.C.

Declaration of Interests

The authors declare no competing interests.

1 Supplementary Materials and methods

All computations were performed using custom MATLAB scripts.

1.1 Analysis of refuge tracking of weakly electric fish in presence of jamming electrodes

In addition to new data collected on electric fish, we examined experimental data of refuge tracking of *Eigenmannia virescens* from a prior study [3]. In that study, a rectangular refuge was actuated to follow a sinusoidal trajectory of frequency 0.1 Hz and amplitude of 17 mm. The fish position was tracked at 60 Hz. The experiments were conducted in the dark in the presence of a closed-loop jamming system where the frequency of the jamming signals was set to 5 Hz below the electric organ discharge (EOD) frequency of the fish under study. To extract the active exploratory movements from refuge tracking response, we first computed the Fourier transform of the original temporal response of fish, deleted the frequency peak corresponding to the refuge motion (0.1 Hz) from the frequency response, and reconstructed the time domain signal using an inverse Fourier transform. The velocity of the active exploratory component was estimated by scaling the forward difference of position data.

1.2 Analysis of postural sway in humans

The experimental data of human postural sway in the upright stance were acquired from a prior study [25] through the authors. In the original experiment, nine healthy individuals maintained a modified tandem Romberg stance for 4 min. The trials were performed under four different multi-sensory conditions with different combinations of vision and tactile sensing—neither vision nor touch, only vision, only touch, and both vision and touch. In the present study, we analyzed the data for three conditions where the subjects were allowed to utilize vision and/or tactile cues. The mediolateral center of mass data was collected from a sensor attached to each subject's lower back at the level of the fourth or fifth lumbar vertebra. We excluded the data from 2 subjects as too noisy ($N = 7$ were used). The original data was collected at a frame rate of 50 Hz. We subsampled the data at 5 Hz to reduce the noise in the velocity data which was computed from forward differences.

1.3 Analysis of saccadic eye movements in humans

The data were acquired from a prior study [29] investigating eye movements in humans during fixated gaze at a stationary object. In the original study, five subjects with normal or corrected-to-normal vision were used. The subjects were instructed to look at circular stimuli of different levels of Gaussian blur and matched summed intensities on the screen at a distance of 175 cm. The eye movements of the subjects were recorded using an Eyelink 1000 eye tracker. The original data were collected at 1000 Hz, then smoothed by the previous authors using a third-order Savitzky-Golay filter of frame length 21 ms. The prior authors also removed blink periods as well as the data 200 ms before and 300 ms after each blink. In the velocity data we detected and removed a few outliers (velocity value greater 1.5×10^{-5} degree/ ms) most likely caused by measurement errors. In the present study we neglected those outliers (0.05% of the original data).

1.4 Analysis of bilateral eye movements in house mice

The data were acquired from a prior study [24] of eye movements in freely moving house mice, *Mus musculus*, during prey (crickets) capture in a closed arena. Eye tracking and head movement were classified by the authors into two different behavioral phases: (1) approach and (2) non-approach. During the approach phases, the mouse head was oriented towards the cricket (the azimuthal angle was with in $\pm 45^o$) and was moving at a speed over 1 cm/s such that the rate of decrease in the distance between the mouse and the cricket was greater than 10 cm/s. During this approach phase the eye movements were more synchronized whereas in the non-approach phases the eye movements were erratic and often moved in opposite direction. In the present study, we focused on the data during the non-approach phases as the abrupt saccades were not directly related to the tracking of the prey movement to

facilitate its capture. We assumed the exploratory eye movements during the non-approach phase were largely driven by the need for sensing. The approach phase behaviors were short ($\approx 5.8\%$ of the whole dataset) whereas non-approach segments were long and more frequent. The original dataset has 105 trajectories collected from seven subjects at frame rate 30 Hz. The data contained some discontinuities due to tracking loss. We used the moving a median method with window length 30 samples to fill those missing data. The eye velocity data was computed from forward differences.

1.5 Analysis of pinnae movements in big brown bats

The echolocation data were acquired from a prior study [24] of the pinnae movement in big brown bats, *Eptesicus fuscus*, in relation to the prey trajectories. The prey target used were mealworms tethered to a wire which was moved toward the bats resting on a platform. For the current analysis, we considered two scenarios out of four originally presented in [24]: (1) single-target simple-trajectory (Extended Data Fig. 9b left) and (2) single-target complex-trajectory (Extended Data Fig. 9b right). Initial target distance for all cases was 2.5 m away from the position of the bats. The single-target simple-trajectory case involved only forward movement of the target toward the bats whereas in the case of single-target complex-trajectory, the target was moved in a complex fashion—it was receded twice before finally arriving at the bat platform. The dataset has 10 trajectories for each case collected from three subjects at frame rate 500 Hz. The echolocation calls of the bats were classified into two phases—"approach" and "buzz" phases [50]. A sharp drop in the pulse duration and the pulse interval is the indication of the buzz phase and we found in this case the distance threshold 0.5 m roughly correlates to the onset of the buzz phase (Figure 1B,C in [24]). In the present study, we focused on the data during the approach phase only. From the temporal traces of change in the z-positions of the tip of the pinnae, we computed the relative movement (difference between z-positions of left and right pinnae tips). We computed the rate of change of this relative movement using forward differences.

1.6 Analysis of odor tracking in Eastern moles

Blind Eastern moles (*Scalopus aquaticus*) are known for their excellent odor tracking capability. The tracking data of moles locating a stationary odor source (small sections of earthworms) in a semicircular arena were taken from the published dataset of [3] which was digitized from the original study of [22]. Among the three original experimental conditions, we only considered the case of normal airflow. The dataset comprises six trajectories. From the angular position data we subtracted the last frame to align the data with respect to the destination. The frame rate for data collection was not stated in [22]. In [22], the reported usual time for moles to find the odor sources was in the range of 5-10 s and the longest data sequence had of 125 frames. Thus, we set the frame rate to be 25 frames per second when computing the angular velocity using forward differences. Note that a different choice of frame rate would neither affect the shape of the histogram nor our claims about the statistical structure of the data.

1.7 Analysis of odor plume tracking in American cockroach

Plume tracking data of adult male American cockroaches (*Periplaneta americana*) were acquired from the published dataset of [3] which was originally from a prior study [19]. The head position was tracked in male animals during the tracking task of locating the source of female sex pheromone (Periplanone B) in a laminar flow tunnel (with wind speed 25 cm/s) under red and infrared light. To understand the role of the olfactory sensors on the antennae, the authors conducted experiments where either one antenna (unilateral) or both antennae (bilateral) were cut to specific lengths. The original data were collected at a frame rate of 30 Hz, which was later subsampled by the authors at 15 Hz. In the present study, we only considered lateral movement of the head under bilateral conditions.

1.8 Analysis of tactile sensing in Hawkmoths

Crepuscular hawkmoths (*Manduca sexta*) use their proboscis as a tool for an active exploration on the flower surface in search for the nectary. The tactile sensing data were acquired from a prior study [21]

through the published dataset. In the original experiment, the moths were presented with 3-D printed flowers (modeled after corolla), with different cross sectional curvature profiles. We only analyzed data for "funnel", "near-funnel", and "near-flat" shapes for the first and seventh visit of flowers by the moths. In the experiment the tip and bottom of the unfurled proboscis, antennae and the thorax were tracked at a frame rate of 100 Hz. The prior study reported two parameters: (1) normalized relative radial distance (RRD) which was computed as the distance of the proboscis tip from the center of the artificial flower normalized to the radius of the artificial flower; and (2) the relative radial orientation (RRO) angle which was computed as the angle between the proboscis tip trajectory and radial axis which was further wrapped to restrict the range to $0 - 90$ degree. On successful insertion of the proboscis, a sharp decrease in the RRD value was noticed, indicating that the moth started feeding from the nectary. Based on this observation we divided each trials into two phases: pre-feeding and feeding where the transition frame was manually selected by inspection of the data. We only took the tracking data pertinent to the pre-feeding phase and the trials where these two phases were not distinct were discarded from the present analysis. We computed the rate of change of RRO from forward differences.

1.9 Analysis of visual tracking of flower by Hawkmoths

Hawkmoths rely heavily on visual inputs to track a swaying flower, and the lighting conditions affect the tracking behavior [20]. These moths hover during tracking. We analyzed tracking data published in an earlier study [20]. In the original experiment, three species of hawkmoths (nocturnal *Deilephila elpenor*, diurnal *Macroglossum stellatarum*, and crepuscular *Manduca sexta*) were presented with a 3-D printed flower which was actuated by a stepper motor following a sum-of-sine stimulus. The experiments were performed at three different illuminance levels. The datasets were collected at 100 Hz. For the present analysis, we considered the data for 15 and 300 lux. To extract the active exploratory movements from the tracking response, we first computed the Fourier transform of the original temporal response, next removed the frequency peaks corresponding to the flower motion from the frequency response, and finally reconstructed the time domain signal using an inverse Fourier transform. The velocity was estimated from forward differences of position data.

1.10 Analysis of galvanotaxis in amoebae

Galvanotaxis data of amoebae movement were acquired from a prior study [26] through the published dataset. Small groups of amoebae (6 to 8 cells on average) were placed in a custom-made chamber with simplified Chalkley medium. Once a laminar flux was established in the experimental chamber, an electric field was applied with a gradient of 334-342 mV/mm. In the present study we focused on the movement in the transverse direction of the applied electric field. The original dataset was collected at every 10 s interval. The velocity was estimated from forward differences of position data.

Extended Data Figures

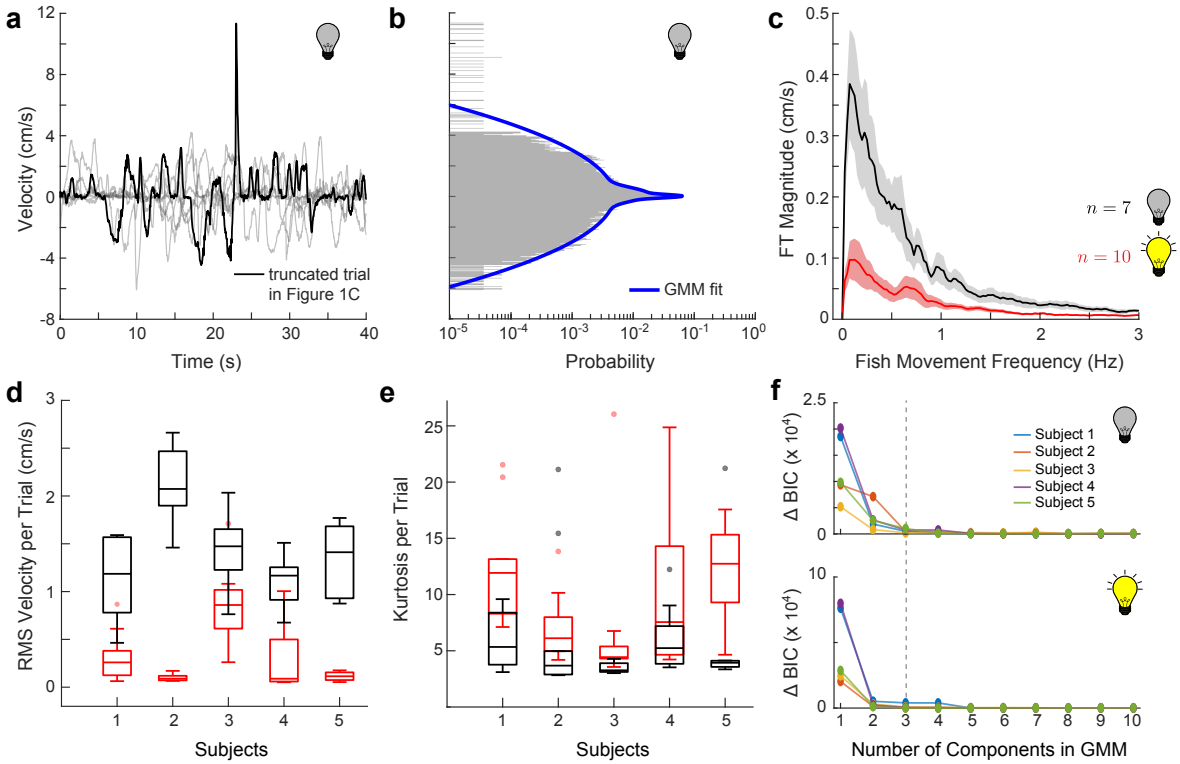

Extended Data Fig. 1. Comparison of fish movement in lights-on trials versus lights-off trials. (a) Velocity trace of the truncated trial data (black) with others (gray) for the individual (Subject 1) from Fig. 1c. (b) Histogram of all trials ($n = 7$) using same length scale, and the three-component Gaussian mixture model (GMM) fit (blue). (c) Magnitude of Fourier transform of velocity traces (black: lights off; red: lights on) with total number of trials (n) indicated next to the plots. The solid line and the shaded region denote mean and the standard error of mean, respectively. (d) Box and whisker plot showing RMS values of individual trials for all subjects ($N = 5$). Colors are same as in (c). Mean RMS velocity across trials for all subjects in lights-off trials was greater than in lights-on trials (one-tailed p-value < 0.005). (e) Box and whisker plot showing kurtosis values of individual trials for all subjects ($N = 5$). Colors are same as in (c). For all subjects, mean kurtosis values across trials in lights-on trials was greater than in lights-off trials (one-tailed p-value < 0.05). (f) Differential Bayesian information criterion (Δ BIC) values for varying number of components in GMM (top: lights off; bottom: lights on) computed as a difference with respect to the minimum BIC value obtained for each subjects. The gray dashed line corresponds to three-component GMM. Colors denote different subjects. All p-values were calculated using the Mann-Whitney-Wilcoxon test.

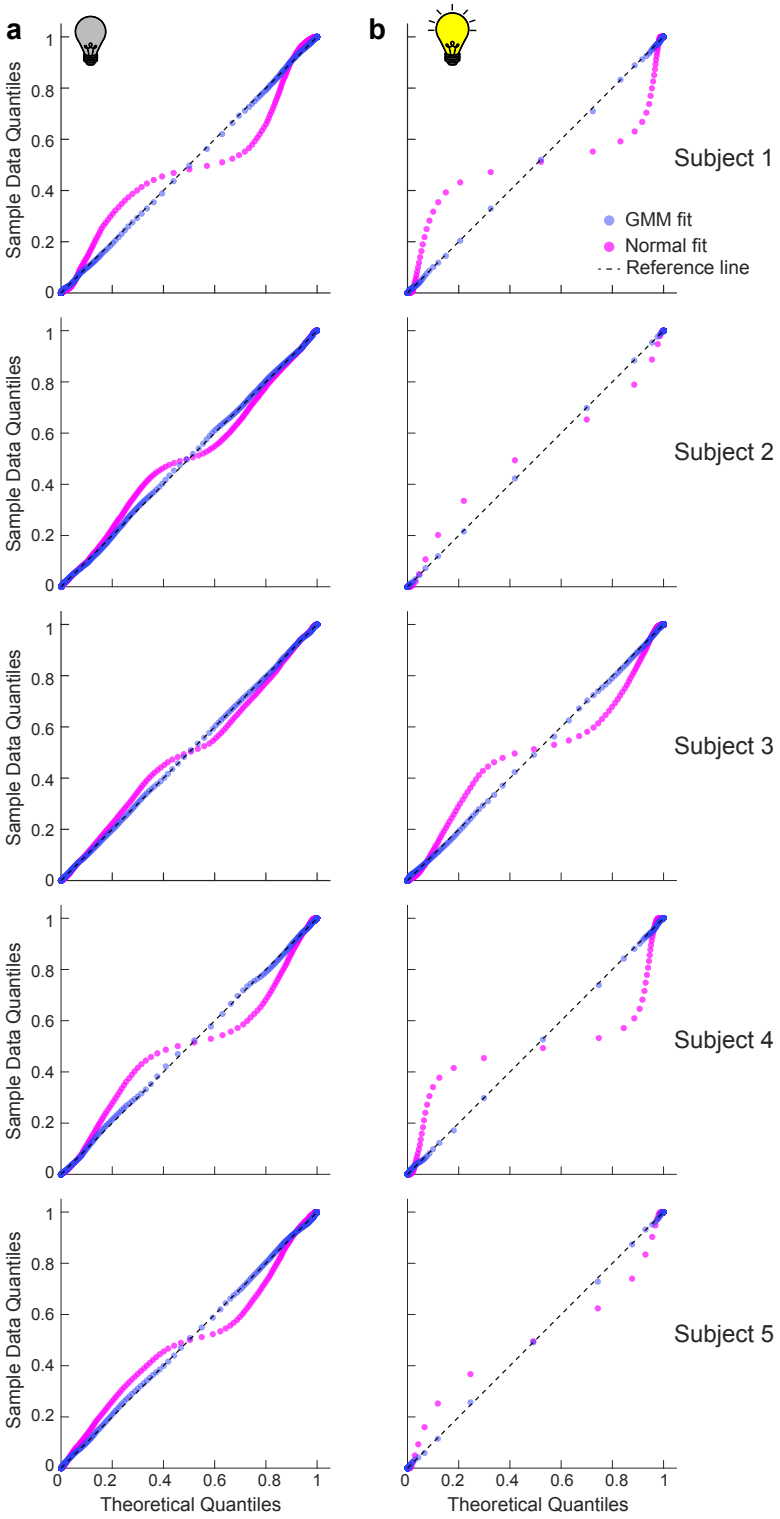

Extended Data Fig. 2. Q-Q plots of velocity traces supported the existence of different behavioral modes. (a,b) Q-Q plots comparing the sample velocity data for all individuals ($N = 5$) from lights-off (a) and lights-on trials (b) with theoretical quantiles from a normal (magenta) and GMM fit (blue), respectively. Lesser deviation from the reference line (black dashed) for GMM fits with three components suggested better fitting. The Q-Q plots also suggested that the lights-off trial data were closer to respective normal distribution fits than those of lights-on trial data.

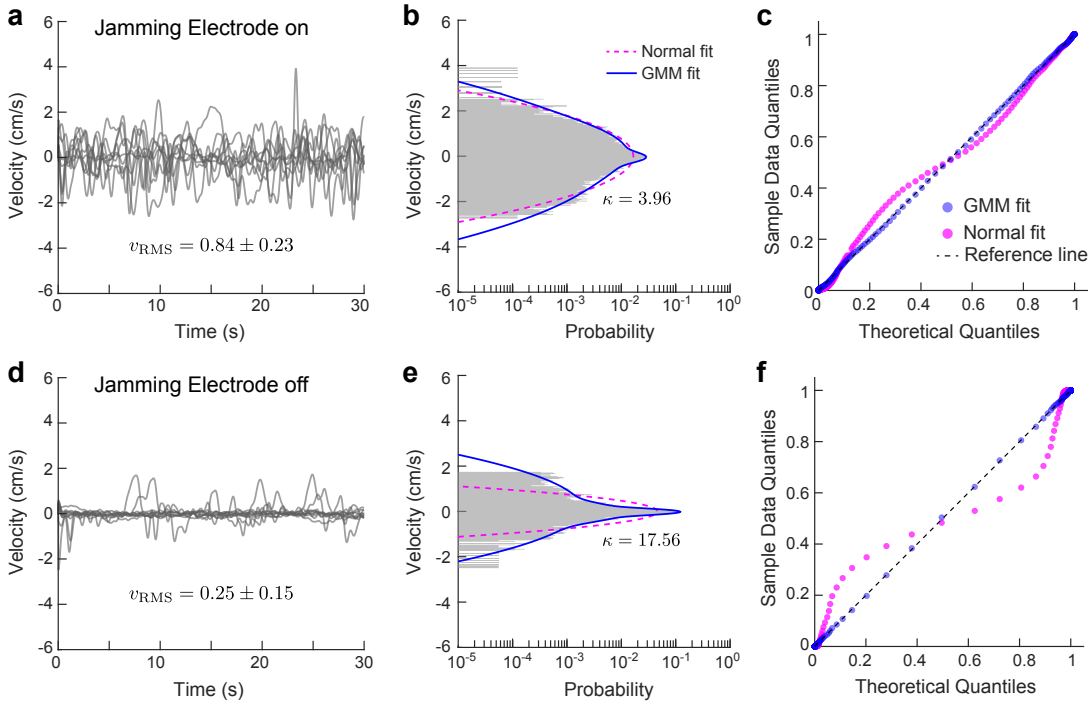

Extended Data Fig. 3. Analysis of the experimental data from *Eigenmannia virescens* [3] with jamming electrodes reveals similar trends in velocity distributions. (a) Velocity traces ($n = 10$) with electrical "jamming" of the fish electrosensory system, which decreased the salience and reliability of electrosensory navigation. (b) Corresponding histogram, with the kurtosis value, κ. The magenta dashed and the blue curves correspond to a normal and GMM fit with three components, respectively. (c) Q-Q plots comparing the sample velocity data for all trials ($n = 10$) from (a) with theoretical quantiles from the same normal (magenta) and GMM fit (blue) from (b). Clearly, the GMM fit was better than the normal. See Extended Data Table 2 for statistical details. (d–f) Velocity traces ($n = 10$) with jamming electrode off (d), corresponding histogram (e) with the kurtosis value, κ and the Q-Q plots (f). Colors and styles are same as in (a–c). Mean $\pm$ SD of the respective RMS values of velocity (v_{RMS}) are shown next to plots of (a,d).

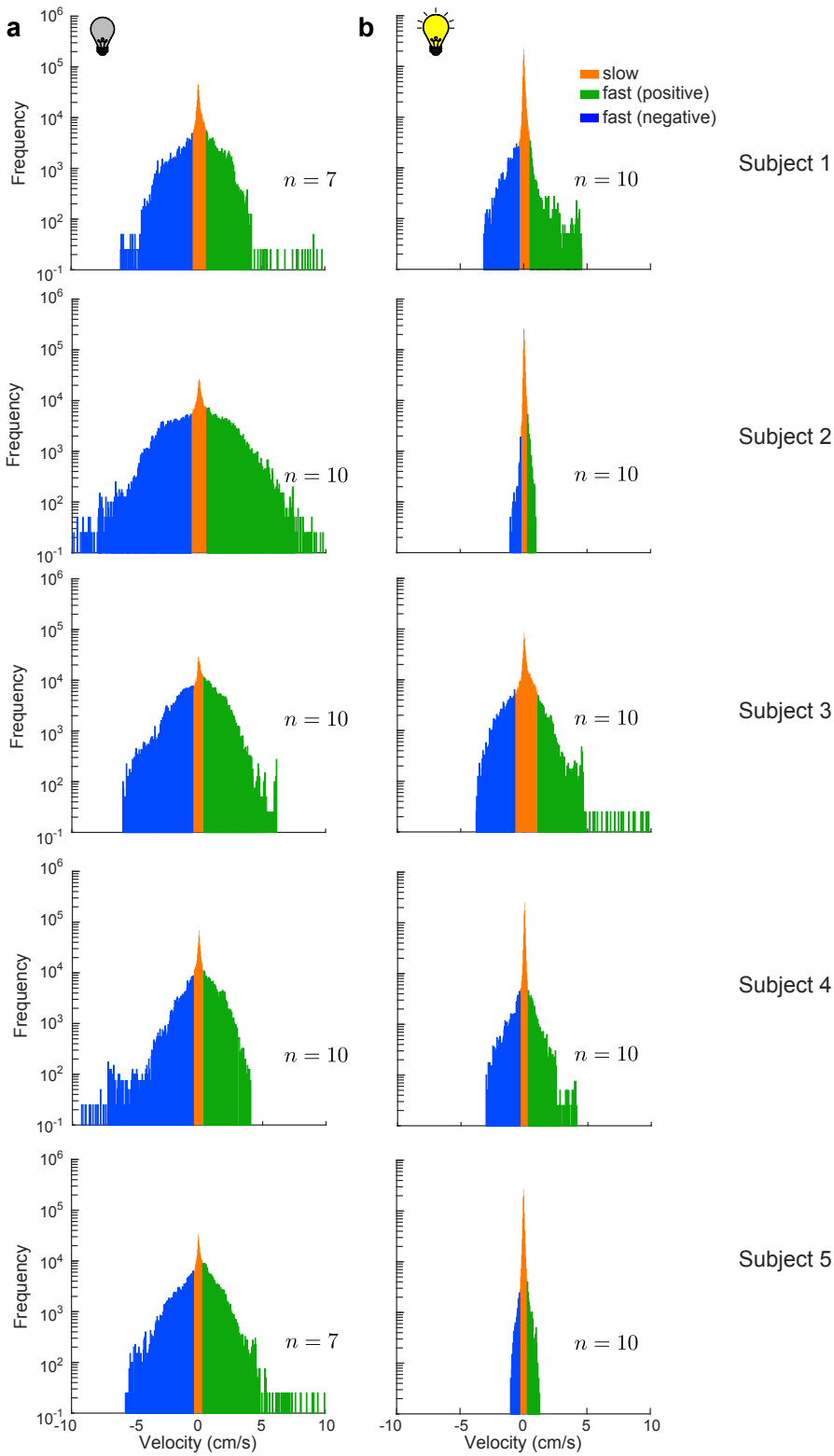

Extended Data Fig. 4. Clustering of velocity data into different behavioral modes. (a,b) Velocity histograms of lights-off (a) and lights-on (b) trials with three clusters: slow (orange), fast positive (green) and fast negative (blue). The clustering was based on a velocity threshold algorithm (see Methods for details).

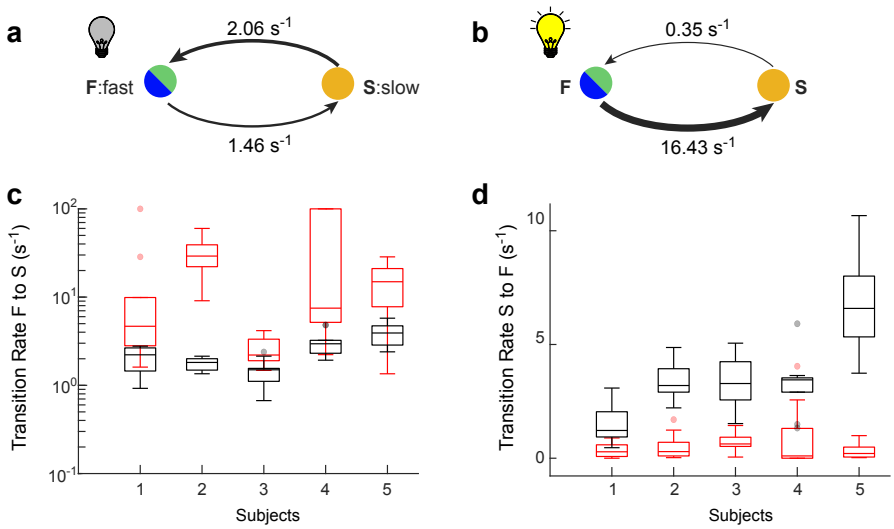

Extended Data Fig. 5. Two-state Markov model and transition rates. (a,b) Two-state (F: fast velocity both positive and negative combined and S: slow velocity) Markov process showing mean transition rates for a representative individual in lights-off (a) and lights-on trials (b). (c,d) Transition rates corresponding to state transitions: F $\rightarrow$ S in (c) and S $\rightarrow$ F in (d), respectively for lights-on (red) and lights-off (black) trials. The transition rate for F $\rightarrow$ S was higher in lights-on trials (one-tailed p-value ≤ 0.02) whereas the rate for S $\rightarrow$ F was higher in lights-off trials (one-tailed p-value < 0.003). All p-values were calculated using the Mann-Whitney-Wilcoxon test.

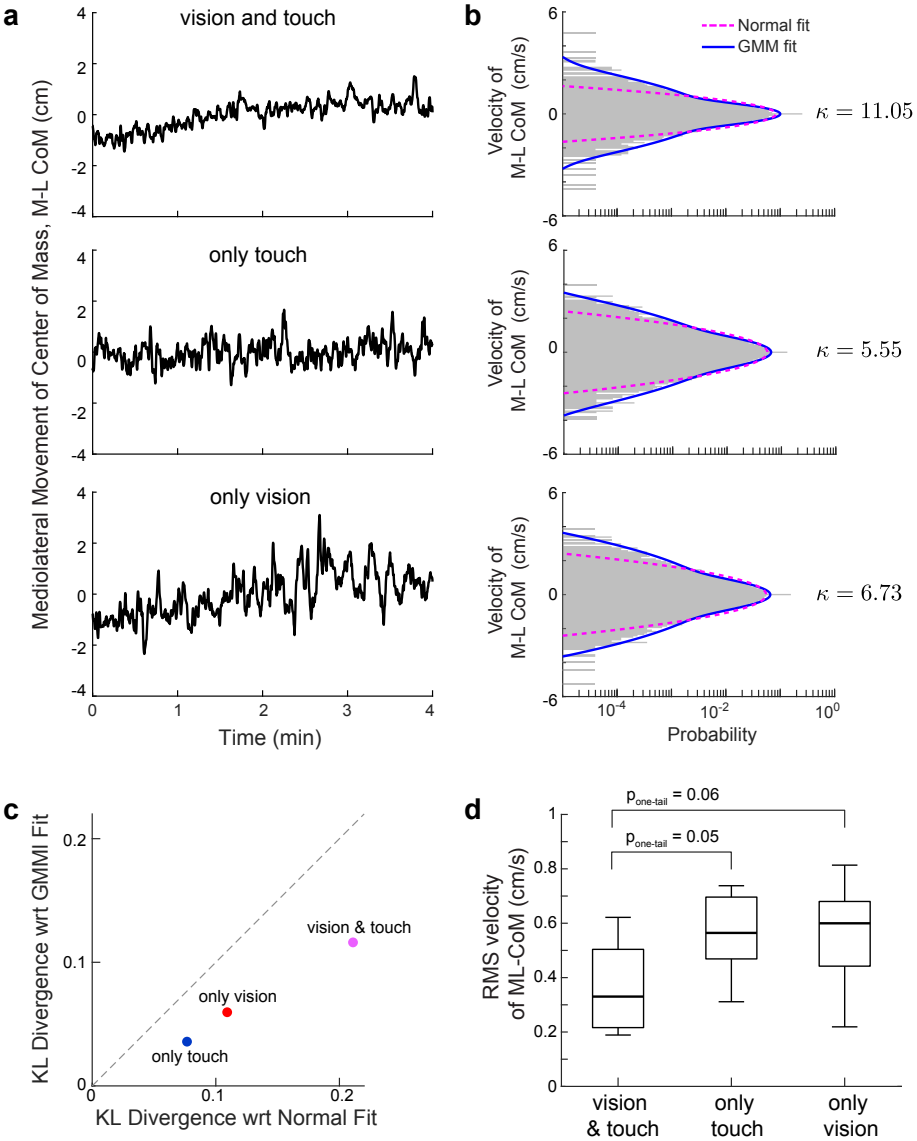

Extended Data Fig. 6. Reanalysis of the postural sway in humans, *Homo sapiens* from [25]. (a,b) Representative temporal traces of mediolateral movement of center of mass, M-L CoM (a) and the histograms of M-L CoM velocities (b) for different experimental conditions—both vision and touch (top), only touch (middle) and only vision (bottom). The magenta dashed and the blue curves in (b) correspond to a normal and GMM fit with three components, respectively. The dataset analyzed here, comprised of 7 subjects, with three replicate trials per experimental condition, was collected at 50 Hz. (c) Plot of K-L divergence values for GMM fit vs Normal fit. Colors denote different experimental conditions. All the markers lying below the unity slope line indicated that the GMM better approximated the data. (d) Comparison of the RMS velocities for different experimental conditions. The one-tailed p-values were computed using the Mann-Whitney-Wilcoxon test.

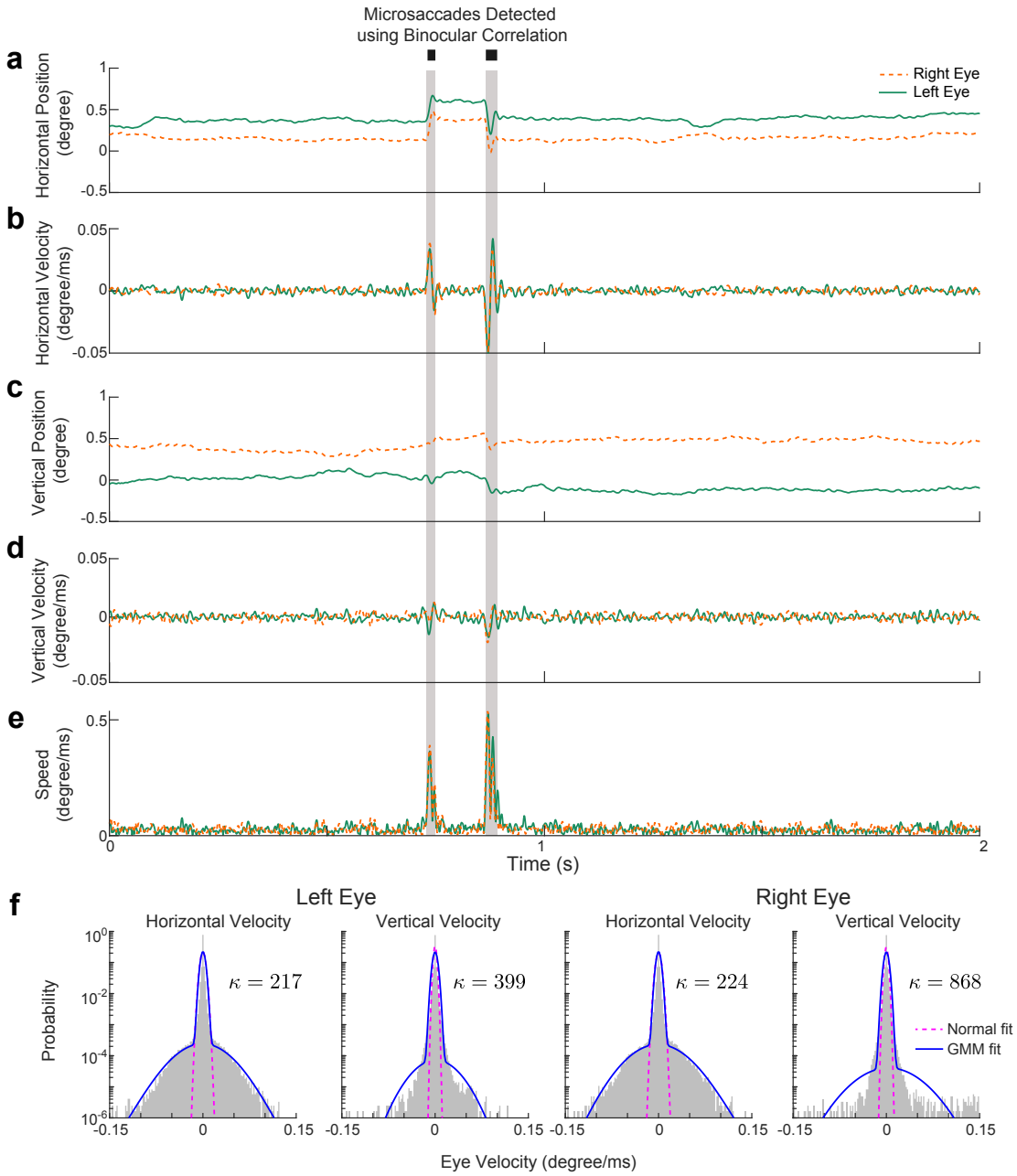

Extended Data Fig. 7. Reanalysis of the gaze fixation in humans, *Homo sapiens* from [29]. (a–e) Representative temporal traces of horizontal eye position (a) and velocity (b), vertical eye position (c) and velocity (d), and eye speed (e) of right (orange dashed) and left (green) eye. The gray sections denote the detected microsaccades using the binoculer correlation (BC) method proposed in [29]. (f) Velocity histograms of horizontal and vertical velocities of left and right eye with respective kurtosis (κ) values. The magenta dashed and the blue curves correspond to a normal and GMM fit with three components, respectively. The dataset was collected from five subjects at 1000 Hz.

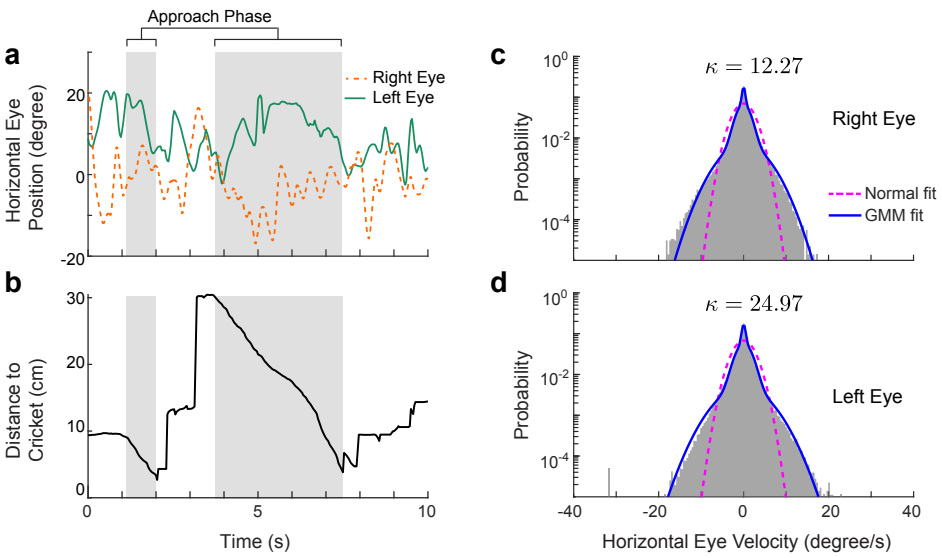

Extended Data Fig. 8. Reanalysis of the bilateral eye movements in house mice, *Mus musculus* during prey capture from [23]. (a) Representative temporal traces of horizontal eye positions of right (orange dashed) and left (green) eye. (b) Representative plot of distance between the mouse and the cricket over time. The grey boxes denote the approach phases during which the mouse head was oriented towards the cricket (the azimuthal angle was with in $\pm 45^o$) and was moving at a speed over 1 cm/s such that the rate of decrease in the distance between the mouse and the cricket was greater than 10 cm/s. For the present study, we focused on the data during the non-approach phases ($\sim$ 95% of the total data). (c,d) Histograms of horizontal eye velocities of right (c) and left (d) eye during the non-approach phases with respective kurtosis (κ) values. The magenta dashed and the blue curves correspond to a normal and GMM fit with three components, respectively. The dataset has 105 trajectories, collected from seven subjects at 30 Hz.

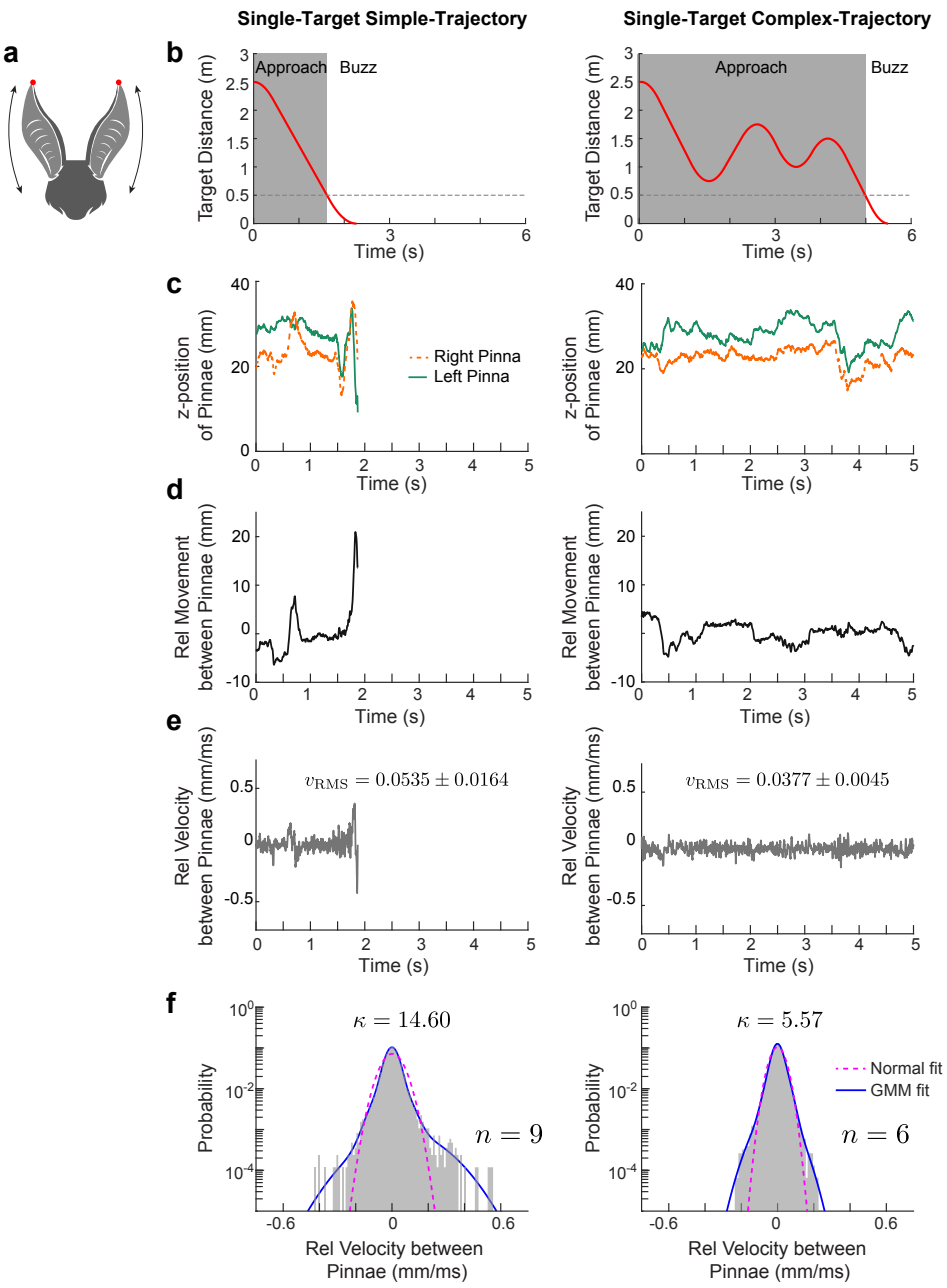

Extended Data Fig. 9. Reanalysis of the tip of the pinnae movement in big brown bats, *Eptesicus fuscus* from [24]. (a) Cartoon showing the "head-waggle" behavior where bat changes the relative z-positions of the tip of its pinnae (red dots). (b) The simple (left) and the complex trajectory (right) of the tethered target (mealworm) over time. The gray box denotes the "approach" phase during which the target distance was greater than 0.5 m (dashed line). The rest we considered as the "buzz" phase. A sharp drop in the pulse duration and the pulse interval marked the beginning of the buzz phase and we found that the distance threshold 0.5 m roughly correlates to the onset of the buzz phase. For the present study, we focused on the data during the approach phase only (ignoring the last 200 frames). (c-f) Representative temporal traces of change in the z-positions (c) of the tip of the pinnae (orange dashed: right pinna, green: left pinna), relative movement (difference in z-positions) between pinnae (d), relative velocity between pinnae (e), and the histograms of relative velocity (f) with respective kurtosis (κ) values and the total number of trials (n) analyzed for the cases of the simple (left) and the complex trajectories (right). Mean $\pm$ SD of the RMS values of the relative velocity (v_{RMS}) are shown next to plots in (e). The one-tailed p-value $= 0.004$ for v_{RMS}, was computed using the Mann-Whitney-Wilcoxon test. The magenta dashed and the blue curves in (f) correspond to a normal and GMM fit with three components, respectively. The dataset has trajectories collected from three subjects at 500 Hz.

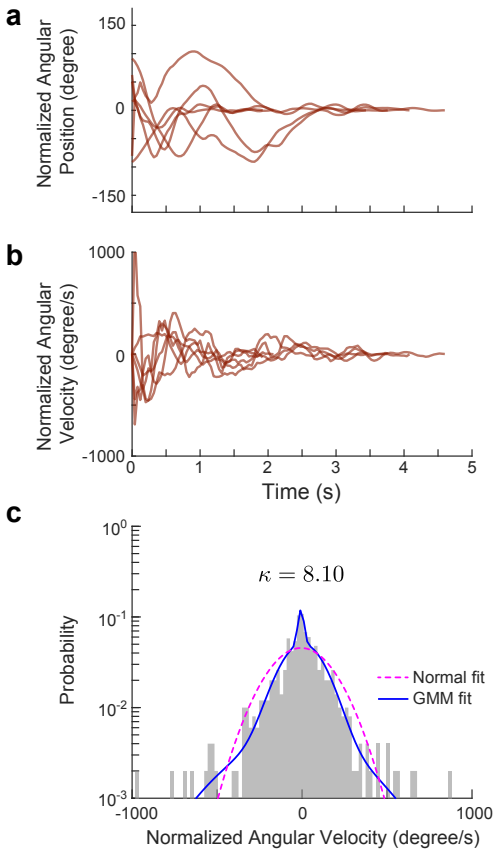

Extended Data Fig. 10. Reanalysis of the olfactory response in Eastern moles, *Scalopus aquaticus* from [22]. (a) Temporal traces ($n = 6$) of angular position of moles normalized such that the destination direction was 0°. (b) Plot of angular velocity assuming the data was sampled at 25 frames per second. (c) Histograms of angular velocities with the kurtosis (κ) value. The magenta dashed and the blue curves correspond to a normal and GMM fit with three components, respectively.

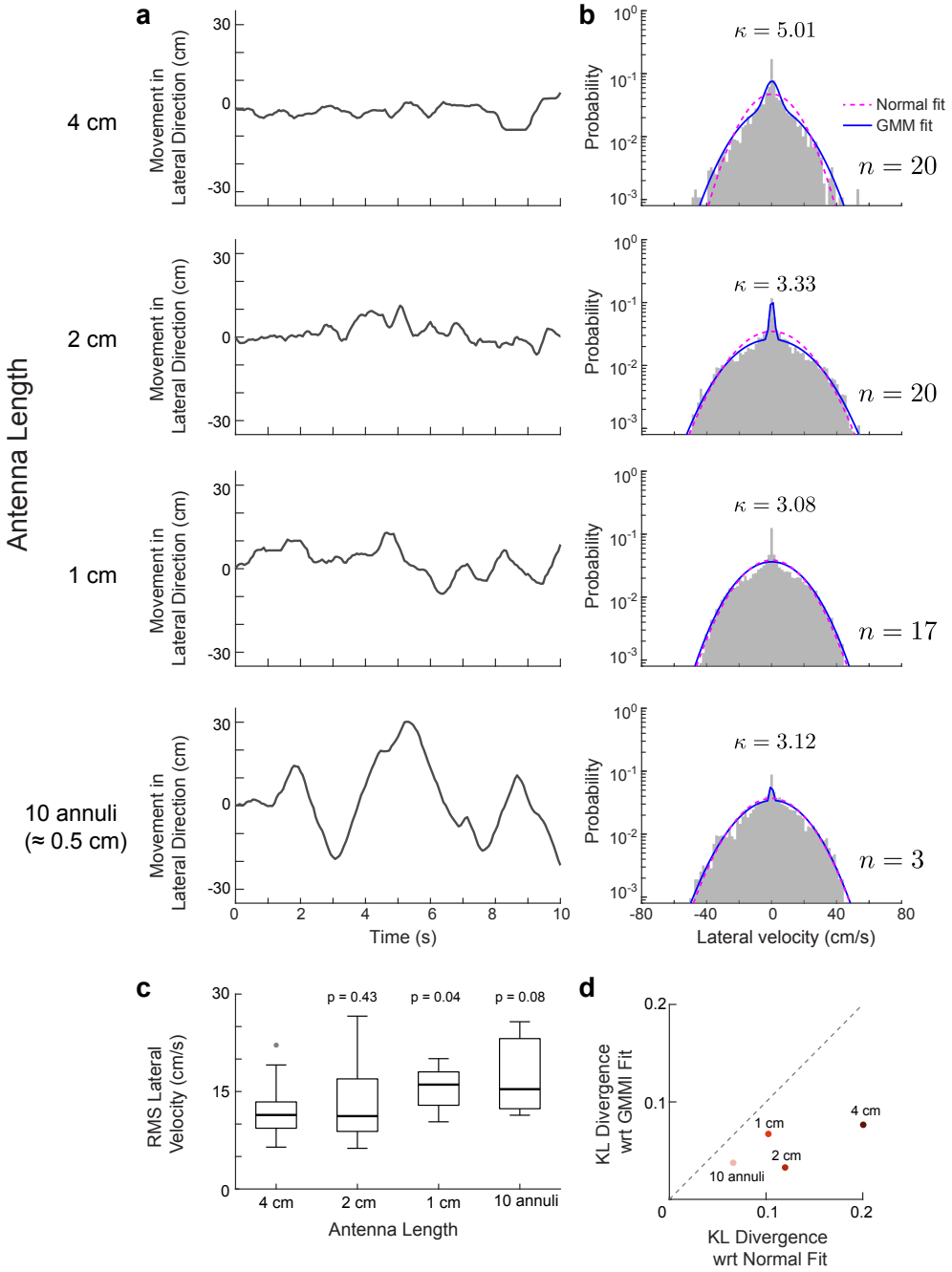

Extended Data Fig. 11. Reanalysis of the odor plume tracking response of American cockroach, *Periplaneta americana* from [19]. (a,b) Representative temporal traces of the lateral head movement (a) and the histograms of the lateral velocities (b) for different antennae length as indicated. The magenta dashed and the blue curves in (b) correspond to a normal and GMM fit with three components, respectively. The dataset analyzed here, was collected at 30 Hz but later was subsampled at 15 Hz by the original study authors. The kurtosis (κ) values and the total number of trajectories (n) analyzed are indicated next to the respective panels in (b). (c) Comparison of the RMS lateral velocities for different experimental conditions. The one-tailed p-values were computed using the Mann-Whitney-Wilcoxon test with respect to the control case: 4 cm (intact antennae). (d) Plot of K-L divergence values for GMM fit vs Normal fit. Colors denote different experimental conditions. All the markers lying below the unity slope line indicated that the GMM better approximated the data.

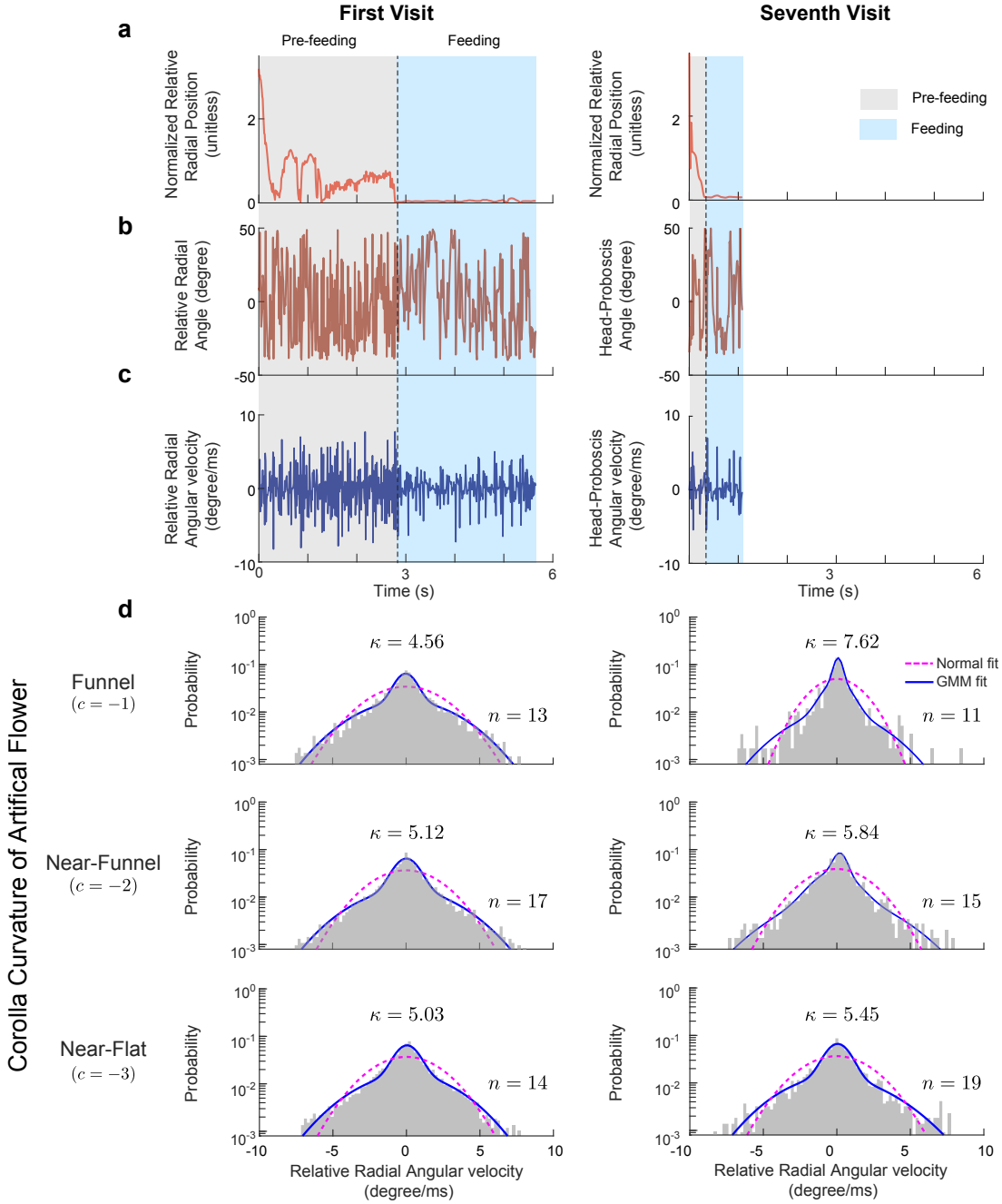

Extended Data Fig. 12. Reanalysis of the tactile response in crepuscular hawkmoth, *Manduca sexta* from [21]. (a-c) Representative temporal traces of the normalized relative radial position (a), the relative radial orientation angle (b), and the relative radial angular velocity (c) during the first visit (left) and the seventh visit (early-learning; right) of the "funnel" type artificial flower by the hawkmoth. The gray and light blue boxes denote the pre-feeding and feeding phases, respectively. The dataset analyzed here was collected at 100 Hz. For the present study, we focused on the data during the pre-feeding phases only. (d) Histograms of relative radial angular velocity for different shape of the flower as indicated. "c" is the curvature parameter for the description of the lateral traces of the corollas. The magenta dashed and the blue curves in (d) correspond to a normal and GMM fit with three components, respectively. The kurtosis (κ) values and the total number of trajectories (n) analyzed are indicated next to the respective panels in (d).

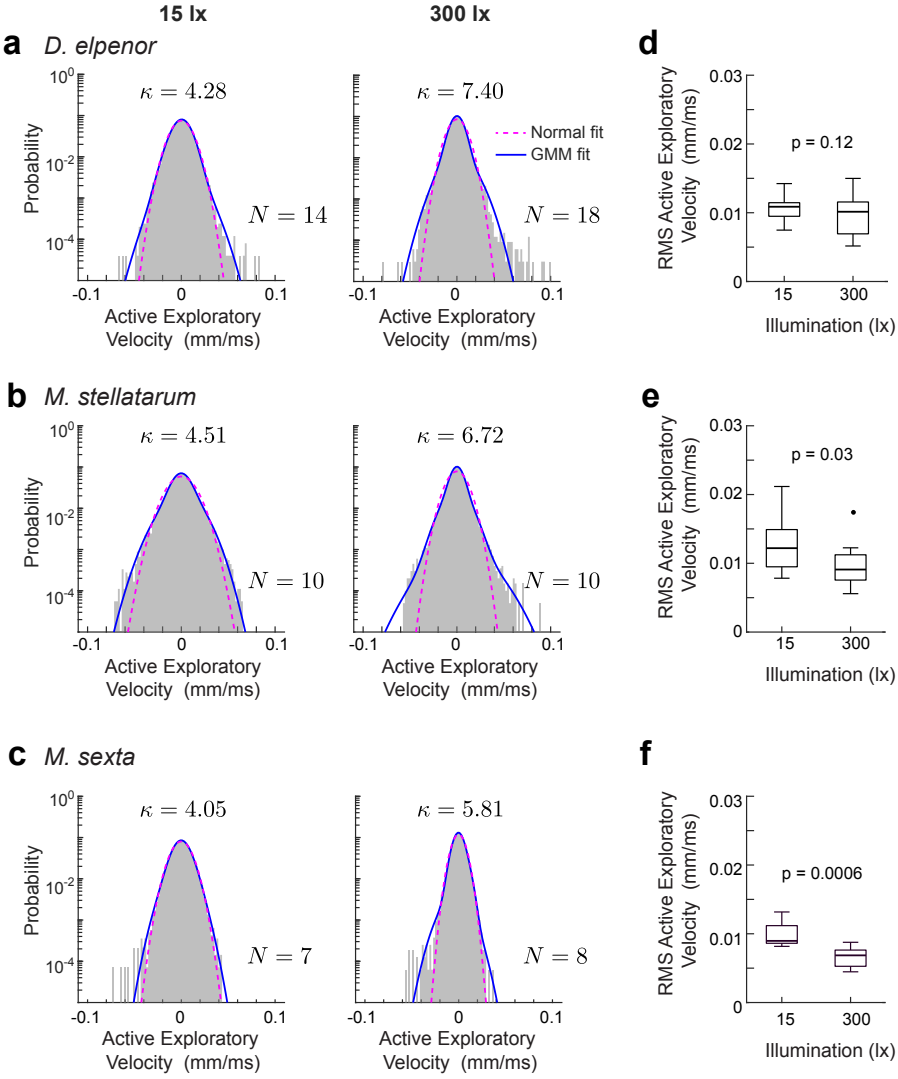

Extended Data Fig. 13. Reanalysis of the active exploratory movement of three different species of hawkmoths during flower tracking from [20]. (a-c) Histograms of active exploratory velocity at low (left: 15 lx) and high (high: 300 lx) illumination level in three different species of hawkmoth—nocturnal *Deilephila elpenor* (A), diurnal *Macroglossum stellatarum* (b), and crepuscular *Manduca sexta* (c). The magenta dashed and the blue curves correspond to a normal and GMM fit with three components, respectively. The kurtosis (κ) values and the total number of subjects (N) analyzed are indicated. (d-f) Box and whisker plots showing the RMS active exploratory velocity for all subjects analyzed at different illumination levels. The one-tailed p-values were computed using the Mann-Whitney-Wilcoxon test. The datasets analyzed here were collected at 100 Hz with one trial per moth ($N = n$).

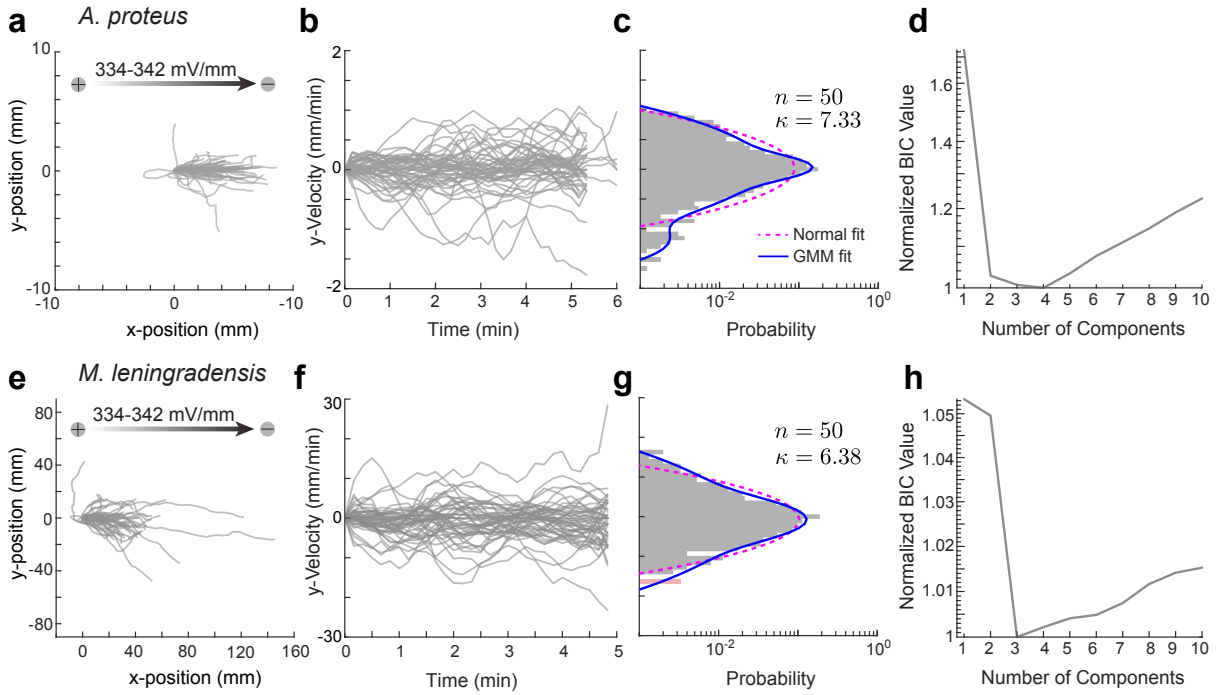

Extended Data Fig. 14. Reanalysis of the directed movement of *Amoeba proteus* and *Metamoeba leningradensis* in response to an electric field (galvaontaxis) from [26]. Migration trajectories ($n = 50$) of *A. proteus* (a), temporal traces of velocities (b) in the transverse direction of the applied electric field derived from the migration data, and the corresponding velocity histogram (c) with kurtosis (κ) value. The magenta dashed and the blue curves in (c) correspond to a normal and GMM fit with three components, respectively. (d) Plot of normalized Bayesian information criterion (BIC) value for varying number of components in the GMM model computed as a ratio with respect to the minimum BIC value obtained. (e-h) Galvanotaxis response in *M. leningradensis*. The panels are same as in (a-d). Image data for both datasets were collected at 0.1 Hz.

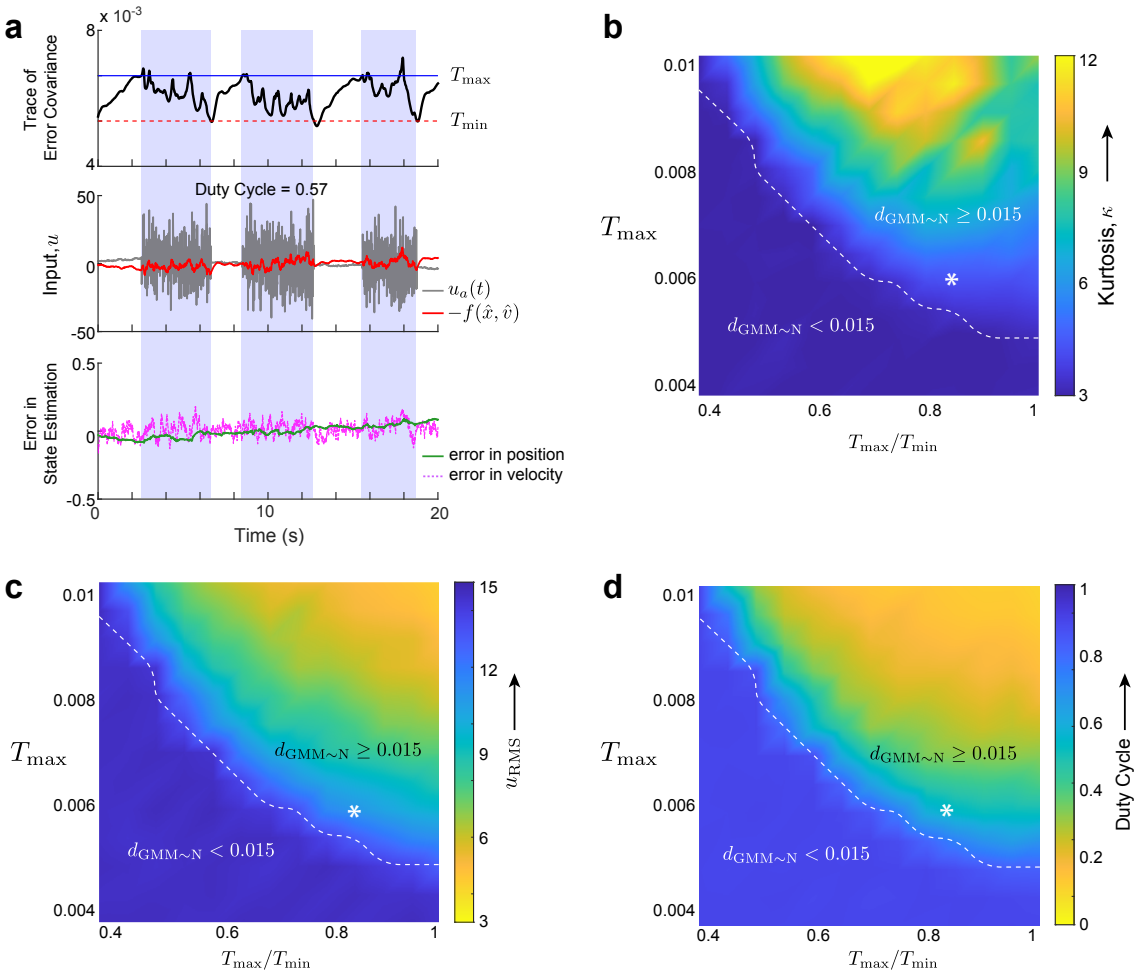

Extended Data Fig. 15. Triggered excitation scheme and the effect of excitation thresholds, $T_{\min}$ and $T_{\max}$. (a) Temporal traces of the trace of the error covariance (M_ε) with threshold levels $T_{\min} = 0.005$ and $T_{\max} = 0.006$ (top), input u (middle; active control component, $u_a(t)$: gray; state-feedback component, $-f(\hat{x},\hat{v})$: red), and the state estimation errors (bottom) in position (green solid) and velocity (magenta dashed). The light blue boxes indicate the triggering instants. The triggering started as the trace of the error covariance exceeded $T_{\max}$ and the triggering continued till the trace of the error covariance dropped below $T_{\min}$. (b–d) Heatmaps showing kurtosis, κ (b) of the velocity distributions, RMS input energy, u_{RMS} (c), and the duty cycle of the input signal as thresholds $T_{\min}$ and $T_{\max}$ were varied. $T_{\max}$ was varied linearly from 0.004 to 0.01 where $T_{\min}$ was varied as the fraction of $T_{\max}$ from 0.4 to 1. From the left to right the relative difference between the thresholds decreased and finally merged to single threshold ($T_{\min} = T_{\max}$) at the end. The white dashed line in (b–d) shows the phase transition based on the absolute difference in the K-L divergences of normal and GMM fit to velocity distributions ($d_{GMM\sim N} = |D_{KL}(V||F_N) - D_{KL}(V||F_{GMM})|$). The region below the line corresponds to $d_{GMM\sim N} < 0.015$ and the region above corresponds to $d_{GMM\sim N} \geq 0.015$. Hence, the region above the line indicates the threshold pairs resulting velocity distributions were better fitted by GMM models. The asterisks denote the threshold values ($T_{\min} = 0.005, T_{\max} = 0.006$) used in (a).

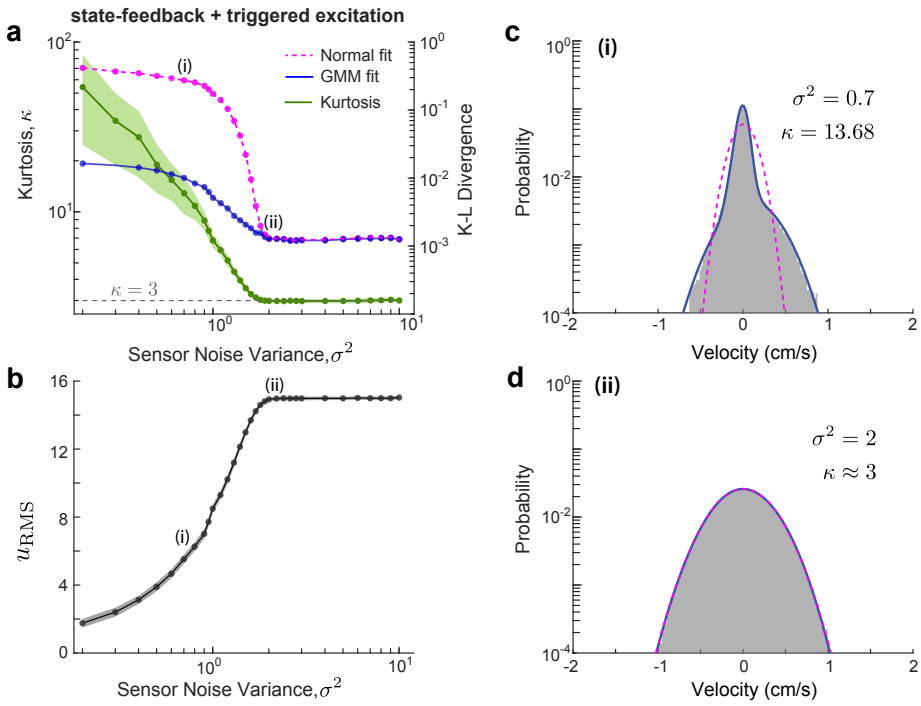

Extended Data Fig. 16. Velocity distribution tends toward a single-component Gaussian with increasing sensor noise in the model. (a) Variation of kurtosis, κ (green, left y-axis), and Kullback–Leibler (K-L) divergence (right y-axis) of normal distribution (magenta dashed) and Gaussian mixture model (blue solid) fit to the velocity distribution with sensor noise variance, σ^2. (b) Variation of RMS input with sensor noise variance, σ^2. The shaded regions in (a,b) denote the respective standard deviations ($n = 25$ independent simulations per σ^2). (c,d) Velocity histograms with kurtosis values are shown for sensor noise variance, $\sigma^2 = 0.70$ and 2, respectively, as indicated by (i) and (ii) in (a,b).

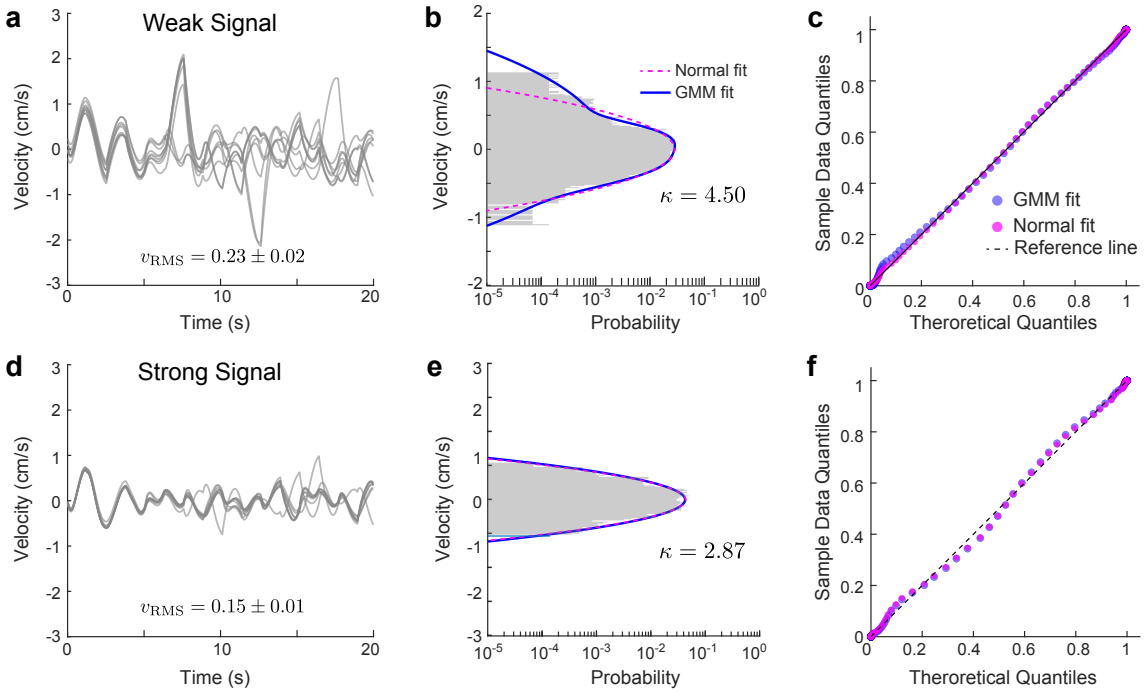

Extended Data Fig. 17. Reanalysis of the simulated trajectories for *Eigenmannia virescens* using Ergodic Harvesting Information (EIH) algorithm from [3]. (a,b) Velocity traces ($n = 9$) for weak signal (a; SNR $\leq$ 30 dB equivalent to jamming amplitude $\geq$ 10 mA) and the corresponding histogram (b) with the kurtosis (κ) value. The magenta dashed and the blue curves correspond to a normal and Gaussian mixture model (GMM) fit with three components, respectively. (c) Q-Q plots comparing the sample velocity data for all trials ($n = 9$) from (a) with theoretical quantiles from the same normal (magenta) and GMM fit (blue) from (b). The fitting performances of GMM and the normal distribution were comparable. See Extended Data Table 4 for statistical details. (d–f) Velocity traces ($n = 9$) for strong signal (d; SNR $\geq$ 50 dB), corresponding histogram (e) with the kurtosis value, and the Q-Q plots (f). Colors and styles are same as in (a–c). Mean $\pm$ SD of the respective RMS values of the velocity (v_{RMS}) are shown on the panels (a,d).

Extended Data Tables

Extended Data Table 1: Comparison of Kullback–Leibler (K-L) divergence and Bayesian information criterion (BIC) for the normal and the three-component Gaussian mixture model (GMM) fits to the velocity data of weakly electric fish, *Eigenmannia virescens*. BIC values are rounded to four significant figures. Relatively lower values of K-L divergence and BIC favors the model.

			Subject Index				
			1	2	3	4	5
lights off	Normal	K-L Divergence	0.346	0.107	0.075	0.261	0.162
		BIC ($\times 10^4$)	9.064	17.50	14.57	12.30	9.641
	GMM	K-L Divergence	0.026	0.017	0.013	0.021	0.027
		BIC ($\times 10^4$)	7.255	16.61	14.07	10.36	8.761
lights on	Normal	K-L Divergence	0.949	0.268	0.315	0.991	0.363
		BIC ($\times 10^4$)	3.943	−7.464	10.80	4.163	−5.506
	GMM	K-L Divergence	0.049	0.058	0.024	0.055	0.051
		BIC ($\times 10^4$)	−3.573	−9.482	8.428	−3.780	−8.373

Extended Data Table 2: Summary of the reanalysis of the published data across different vertebrate species [3, 22–25] showing kurtosis (κ), Kullback–Leibler (K-L) divergence and Bayesian information criterion (BIC) for the normal and the three-component Gaussian mixture model (GMM) fits to the velocity data.

				K-L Divergence		BIC ($\times 10^4$)		
Species	Sensory process	Variables	Cases	GMM	Normal	GMM	Normal	Kurtosis (κ)
Human (*Homo sapiens*)	postural sway [25]	Vel. of mediolateral center of mass	vision+touch	0.1161	0.2110	1.8477	2.3284	11.05
			vision	0.0596	0.1092	4.1721	4.4287	6.73
			touch	0.0358	0.0767	4.2073	4.4115	5.55
Human (*Homo sapiens*)	saccadic eye movement [29]	Horz. vel. of left eye		1.9921	2.3499	−2782	−2674	216.78
		Horz. vel. of right eye		1.9937	2.3720	−2782	−2669	223.98
		Vert. vel. of left eye		1.9826	1.8007	−2782	−2760	398.70
		Vert. vel. of right eye		1.9825	1.8223	−2783	−2746	868.06
House mice (*Mus musculus*)	bilateral eye movement [23]	Horz. vel of left eye	non-approach	0.0230	0.2215	1.4644	1.6259	24.97
		Horz. vel of right eye	non-approach	0.0226	0.2204	1.4464	1.6020	12.27
Big brown bat (*Eptesicus fuscus*)	Pinnae movement during echolocation [24]	Rate of change of relative z-position between pinnae	single-target simple-trajectory	0.0137	0.1639	−2.7253	−2.4706	14.60
			single-target complex-trajectory	0.0119	0.0483	−5.7678	−5.6557	5.57
Eastern mole (*Scalopus aquaticus*)	olfactory driven head movement [22]	Angular velocity	two nostrils open	0.0902	0.2464	0.6482	0.6607	8.10
Weakly electric fish (*Eigenmannia virescens*)	active exploration (during refuge tracking) [3]	Horz. vel. of fish	jamming signal off	0.0233	0.5030	−1.3497	0.4103	17.56
			jamming signal on	0.0147	0.0598	4.0188	4.1790	3.96

Extended Data Table 3: Summary of the reanalysis of the published data across different invertebrate species [19–21] showing kurtosis (κ), Kullback–Leibler (K-L) divergence and Bayesian information criterion (BIC) for the normal and the three-component Gaussian mixture model (GMM) fits to the velocity data.

				K-L Divergence		BIC ($\times 10^4$)		
Species	Sensory process	Variables	Cases	GMM	Normal	GMM	Normal	Kurtosis (κ)
American cockroach (*Periplaneta americana*)	Odor plume tracking [19]	Lateral head velocity	4 cm (intact antennae)	0.0757	0.1997	2.1332	2.2367	5.01
			2 cm	0.0318	0.1189	7.5817	7.7385	3.33
			1 cm	0.0662	0.1016	8.2757	8.4790	3.08
			10 annuli	0.0366	0.0652	2.6725	2.6903	3.12
Hawkmoth (*Manduca sexta*)	tactile sensing [21]	Relative radial angular velocity	1st visit: Funnel	0.0190	0.1142	9.2494	9.3431	4.56
			1st visit: Near-funnel	0.0154	0.1243	14.992	15.170	5.12
			1st visit: Near-flat	0.0158	0.1138	10.676	10.790	5.03
			7st visit: Funnel	0.0750	0.3288	1.0008	1.0283	7.62
			7st visit: Near-funnel	0.0316	0.1807	2.5886	2.6283	5.84
Hawkmoth (*Deilephila elpenor*)	Active exploration (during visual tracking of swaying flower) [20]	Horizontal velocity	15 lux	0.0071	0.0167	30.43	30.47	4.28
			300 lux	0.0120	0.05493	39.05	39.34	7.40
Hawkmoth (*Macroglossum stellatarum*)			15 lux	0.0054	0.0296	22.73	22.81	4.51
			300 lux	0.0088	0.0682	23.97	24.21	6.72
Hawkmoth (*Macroglossum stellatarum*)			15 lux	0.01	0.0162	16.86	16.87	4.05
			300 lux	0.0162	0.0385	17.95	18.01	5.81

Extended Data Table 4: Summary of comparison among different simulation algorithms showing kurtosis (κ), Kullback–Leibler (K-L) divergence and Bayesian information criterion (BIC) for the normal and the three-component Gaussian mixture model (GMM) fits to the simulated velocity data.

Algorithm	Cases	Sensory Noise	K-L Divergence		BIC ($\times 10^4$)		Kurtosis (κ)	$\Delta\kappa$	
			GMM	Normal	GMM	Normal			
Template model for active exploration	Zero Excitation		0.0076	0.0122	-1.7621	-1.7602	3.49	↔	$\kappa \approx 3$ (constant) for low and high noise
	Gaussian Excitation		0.0240	0.0240	0.7730	0.7688	2.94		
	Triggered Excitation	low ($\sigma^2 = 0.5$)	0.0129	0.3063	-2.0478	-1.3962	19.03	↑	κ increases for low noise
		high ($\sigma^2 = 2$)	0.0015	0.0016	0.4569	0.4520	2.93		
Ergodic Information Harvesting [3]†		low (SNR > 50 dB)	0.0479	0.0479	-1.4280	-1.4337	2.87	↓	κ decreases for low noise ‡
		high (SNR ≤ 30 dB)	0.0492	0.0492	-0.2468	-0.1901	4.50		

† We used the same set of parameters specified by the authors in Chen *et al.* [3]. From the simulated refuge tracking response, the active exploration component is extracted following the method (eliminating frequency peak corresponding to the refuge motion) explained in supplementary method. Further work is needed to understand the effect of different parameters of EIH algorithm on the simulated response.

‡ EIH algorithm produces the opposite trend in kurtosis (κ) of velocity distributions in relation to sensory salience as observed in wide range of organisms. [19–26]

References

[1] J. J. Gibson, "Observations on active touch," *Psychol Rev*, vol. 69, no. 6, p. 477, 1962.

[2] D. Biswas, L. A. Arend, S. A. Stamper, B. P. Vágvölgyi, E. S. Fortune, and N. J. Cowan, "Closed-loop control of active sensing movements regulates sensory slip," *Curr Biol*, vol. 28, no. 24, pp. 4029–4036, 2018.

[3] C. Chen, T. D. Murphey, and M. A. MacIver, "Tuning movement for sensing in an uncertain world," *eLife*, vol. 9, p. e52371, 2020.

[4] S. Soatto, "Actionable information in vision," in *Machine learning for computer vision*, pp. 17–48, Springer, 2013.

[5] D. Golovin and A. Krause, "Adaptive submodularity: Theory and applications in active learning and stochastic optimization," *J Artif Intell Res*, vol. 42, pp. 427–486, 2011.

[6] G. F. Cooper, "The computational complexity of probabilistic inference using Bayesian belief networks," *Artif Intell*, vol. 42, no. 2-3, pp. 393–405, 1990.

[7] V. D. Blondel and J. N. Tsitsiklis, "A survey of computational complexity results in systems and control," *Automatica*, vol. 36, no. 9, pp. 1249–1274, 2000.

[8] S. C.-H. Yang, D. M. Wolpert, and M. Lengyel, "Theoretical perspectives on active sensing," *Curr Opin Behav Sci*, vol. 11, pp. 100–108, 2016.

[9] S. A. Stamper, E. Roth, N. J. Cowan, and E. S. Fortune, "Active sensing via movement shapes spatiotemporal patterns of sensory feedback," *J Exp Biol*, vol. 215, no. 9, pp. 1567–1574, 2012.

[10] N. J. Cowan and E. S. Fortune, "The critical role of locomotion mechanics in decoding sensory systems," *J Neurosci*, vol. 27, no. 5, pp. 1123–1128, 2007.

[11] E. Roth, K. Zhuang, S. A. Stamper, E. S. Fortune, and N. J. Cowan, "Stimulus predictability mediates a switch in locomotor smooth pursuit performance for *Eigenmannia virescens*," *J Exp Biol*, vol. 214, no. 7, pp. 1170–1180, 2011.

[12] E. E. Sutton, A. Demir, S. A. Stamper, E. S. Fortune, and N. J. Cowan, "Dynamic modulation of visual and electrosensory gains for locomotor control," *J. R. Soc. Interface*, vol. 13, no. 118, p. 20160057, 2016.

[13] G. J. Rose and J. G. Canfield, "Longitudinal tracking responses of the weakly electric fish, *Sternopygus*," *J Comp Physiol A*, vol. 171, no. 6, pp. 791–798, 1993.

[14] I. Uyanik, S. A. Stamper, N. J. Cowan, and E. S. Fortune, "Sensory cues modulate smooth pursuit and active sensing movements," *Front Behav Neurosci*, vol. 13, p. 59, 2019.

[15] S. Sefati, I. D. Neveln, E. Roth, T. R. Mitchell, J. B. Snyder, M. A. MacIver, E. S. Fortune, and N. J. Cowan, "Mutually opposing forces during locomotion can eliminate the tradeoff between maneuverability and stability," *Proc Natl Acad Sci U.S.A.*, vol. 110, no. 47, pp. 18798–18803, 2013.

[16] K. S. Narendra and A. M. Annaswamy, "Persistent excitation in adaptive systems," *Int J Control*, vol. 45, no. 1, pp. 127–160, 1987.

[17] A. Kunapareddy and N. J. Cowan, "Recovering observability via active sensing," in *Proc Amer Control Conf*, (Milwaukee, WI, USA), pp. 2821–2826, IEEE, 2018.

[18] E. D. Sontag, D. Biswas, and N. J. Cowan, "An observability result related to active sensing," 2022.

[19] J. K. Lockey and M. A. Willis, "One antenna, two antennae, big antennae, small: total antennae length, not bilateral symmetry, predicts odor-tracking performance in the American cockroach *Periplaneta americana*," *J Exp Biol*, vol. 218, no. 14, pp. 2156–2165, 2015.

[20] A. L. Stöckl, K. Kihlström, S. Chandler, and S. Sponberg, "Comparative system identification of flower tracking performance in three hawkmoth species reveals adaptations for dim light vision," *Philos Trans R Soc Lond B Biol Sci*, vol. 372, no. 1717, p. 20160078, 2017.

[21] T. Deora, M. A. Ahmed, T. L. Daniel, and B. W. Brunton, "Tactile active sensing in an insect plant pollinator," *J Exp Biol*, vol. 224, no. 4, p. jeb239442, 2021.

[22] K. C. Catania, "Stereo and serial sniffing guide navigation to an odour source in a mammal," *Nat Commun*, vol. 4, no. 1, pp. 1–8, 2013.

[23] A. M. Michaiel, E. T. Abe, and C. M. Niell, "Dynamics of gaze control during prey capture in freely moving mice," *eLife*, vol. 9, p. e57458, 2020.

[24] M. J. Wohlgemuth, N. B. Kothari, and C. F. Moss, "Action enhances acoustic cues for 3-D target localization by echolocating bats," *PLoS Biol*, vol. 14, no. 9, p. e1002544, 2016.

[25] T. Kiemel, K. S. Oie, and J. J. Jeka, "Multisensory fusion and the stochastic structure of postural sway," *Biol Cybern*, vol. 87, no. 4, pp. 262–277, 2002.

[26] I. M. De la Fuente, C. Bringas, I. Malaina, M. Fedetz, J. Carrasco-Pujante, M. Morales, S. Knafo, L. Martínez, A. Pérez-Samartín, J. I. López, G. Pérez-Yarza, and M. D. Boyano, "Evidence of conditioned behavior in amoebae," *Nat Commun*, vol. 10, no. 1, pp. 1–12, 2019.

[27] M. Fabre, M. Antoine, M. G. Robitaille, E. Ribot-Ciscar, R. Ackerley, J.-M. Aimonetti, P. Chavet, J. Blouin, M. Simoneau, and L. Mouchnino, "Large postural sways prevent foot tactile information from fading: Neurophysiological evidence," *Cereb Cortex Comm*, vol. 2, 12 2020.

[28] K. Arkley, R. A. Grant, B. Mitchinson, and T. J. Prescott, "Strategy change in vibrissal active sensing during rat locomotion," *Curr Biol*, vol. 24, no. 13, pp. 1507–1512, 2014.

[29] A.-K. Hauperich, L. K. Young, and H. E. Smithson, "What makes a microsaccade? A review of 70 years of research prompts a new detection method," *J Eye Mov Res*, vol. 12, no. 6, 2019.

[30] M. Nelson, Z. Xu, and J. Payne, "Characterization and modeling of p-type electrosensory afferent responses to amplitude modulations in a wave-type electric fish," *J Comp Physiol A*, vol. 181, no. 5, pp. 532–544, 1997.

[31] J. Lee, S. N. Sponberg, O. Y. Loh, A. G. Lamperski, R. J. Full, and N. J. Cowan, "Templates and anchors for antenna-based wall following in cockroaches and robots," *IEEE Trans Robot*, vol. 24, no. 1, pp. 130–143, 2008.

[32] N. O. Zweifel and M. J. Hartmann, "Defining "active sensing" through an analysis of sensing energetics: homeoactive and alloactive sensing," *J Neurophys*, vol. 124, no. 1, pp. 40–48, 2020.

[33] T. H. Bullock, "Electroreception," *Annu Rev Neurosci*, vol. 5, pp. 121–170, 1982.

[34] S. Brinkløv, C. P. Elemans, and J. M. Ratcliffe, "Oilbirds produce echolocation signals beyond their best hearing range and adjust signal design to natural light conditions," *R Soc Open Sci*, vol. 4, no. 5, p. 170255, 2017.

[35] M. E. Nelson and M. A. MacIver, "Sensory acquisition in active sensing systems," *J Comp Physiol A*, vol. 192, no. 6, pp. 573–586, 2006.

[36] J. B. Snyder, M. E. Nelson, J. W. Burdick, and M. A. MacIver, "Omnidirectional sensory and motor volumes in electric fish," *PLoS Biol*, vol. 5, no. 11, p. e301, 2007.

[37] K. Ghose and C. F. Moss, "Steering by hearing: a bat's acoustic gaze is linked to its flight motor output by a delayed, adaptive linear law," *J Neurosci*, vol. 26, no. 6, pp. 1704–1710, 2006.

[38] H. C. Berg and D. A. Brown, "Chemotaxis in *Escherichia coli* analysed by three-dimensional tracking," *Nature*, vol. 239, no. 5374, pp. 500–504, 1972.

[39] J. Benda, A. Longtin, and L. Maler, "A synchronization-desynchronization code for natural communication signals," *Neuron*, vol. 52, no. 2, pp. 347–358, 2006.

[40] M. G. Metzen, V. Hofmann, and M. J. Chacron, "Neural synchrony gives rise to amplitude-and duration-invariant encoding consistent with perception of natural communication stimuli," *Front Neurosci*, vol. 14, p. 79, 2020.

[41] V. Hofmann and M. J. Chacron, "Population coding and correlated variability in electrosensory pathways," *Front Integr Neurosci*, vol. 12, p. 56, 2018.

[42] J. Grewe, A. Kruscha, B. Lindner, and J. Benda, "Synchronous spikes are necessary but not sufficient for a synchrony code in populations of spiking neurons," *Proc Natl Acad Sci U.S.A.*, vol. 114, no. 10, pp. E1977–E1985, 2017.

[43] J. R. Fetcho, S.-i. Higashijima, and D. L. McLean, "Zebrafish and motor control over the last decade," *Brain Res Rev*, vol. 57, no. 1, pp. 86–93, 2008.

[44] K. M. Tabor, S. A. Bergeron, E. J. Horstick, D. C. Jordan, V. Aho, T. Porkka-Heiskanen, G. Haspel, and H. A. Burgess, "Direct activation of the Mauthner cell by electric field pulses drives ultrarapid escape responses," *J Neurophysiol*, vol. 112, no. 4, pp. 834–844, 2014.

[45] É. M. Hitschfeld, S. A. Stamper, K. Vonderschen, E. S. Fortune, and M. J. Chacron, "Effects of restraint and immobilization on electrosensory behaviors of weakly electric fish," *ILAR journal*, vol. 50, no. 4, pp. 361–372, 2009.

[46] B. P. Vágvölgyi, "General tracker." `https://github.com/vagvolgyi/general_tracker`, 2021.

[47] M. Matthews and S. Sponberg, "Hawkmoth flight in the unsteady wakes of flowers," *J Exp Biol*, vol. 221, no. 22, p. jeb179259, 2018.

[48] H. M. Tritico and A. J. Cotel, "The effects of turbulent eddies on the stability and critical swimming speed of creek chub *Semotilus atromaculatus*," *J Exp Biol*, vol. 213, no. 13, pp. 2284–2293, 2010.

[49] C. M. Harris and D. M. Wolpert, "Signal-dependent noise determines motor planning," *Nature*, vol. 394, no. 6695, pp. 780–784, 1998.

[50] J. M. Ratcliffe, C. P. Elemans, L. Jakobsen, and A. Surlykke, "How the bat got its buzz," *Biol Lett*, vol. 9, no. 2, p. 20121031, 2013.